The SAMI Galaxy Survey: gas streaming and dynamical M/L in rotationally supported systems

G. Cecil,[1,2]★ L. M. R. Fogarty,[2,3] S. Richards,[2,3,4] J. Bland-Hawthorn,[2] R. Lange,[5] A. Moffett,[5] B. Catinella,[5,6] L. Cortese,[5,6] I.-T. Ho,[7] E. N. Taylor,[8] J. J. Bryant,[2,3,4] J. T. Allen,[2,3] S. M. Sweet,[9] S. M. Croom,[2,3] S. P. Driver,[5] M. Goodwin,[4] L. Kelvin,[10] A. W. Green,[4] I. S. Konstantopoulos,[11] M. S. Owers,[4,12] J. S. Lawrence[4] and N. P. F. Lorente[4]

[1]*Department of Physics and Astronomy, University of North Carolina at Chapel Hill, NC 27510, USA*
[2]*Sydney Institute for Astronomy, School of Physics, University of Sydney, NSW 2006, Australia*
[3]*ARC Centre of Excellence for All-Sky Astrophysics, University of Sydney, Redfern NSW 2016, Australia*
[4]*Australian Astronomical Observatory, PO Box 915, North Ryde, NSW 1670, Australia*
[5]*International Centre for Radio Astronomy Research (ICRAR), School of Physics, The University of Western Australia, Perth, WA 6009, Australia*
[6]*Centre for Astrophysics and Supercomputing, Swinburne University of Technology, Melbourne, VIC 3122, Australia*
[7]*Institute for Astronomy, University of Hawaii, 2680 Woodlawn Drive, Honolulu, HI 96822, USA*
[8]*School of Physics, The University of Melbourne, Parkville, VIC 3010, Australia*
[9]*Research School of Astronomy and Astrophysics, The Australian National University, Canberra, ACT 2611, Australia*
[10]*Institute for Astro- and Particle-Physics, University of Innsbruck, Innsbruck, Austria*
[11]*Envizi Group Suite 213, National Innovation Centre, Australian Technology Park, 4 Cornwallis Street, Eveleigh NSW 2015, Australia*
[12]*Department of Physics and Astronomy, Macquarie University, NSW 2109, Australia*

ABSTRACT

Line-of-sight velocities of gas and stars can constrain dark matter (DM) within rotationally supported galaxies if they trace circular orbits extensively. Photometric asymmetries may signify non-circular motions, requiring spectra with dense spatial coverage. Our integral-field spectroscopy of 178 galaxies spanned the mass range of the Sydney-AAO Multi-object integral field spectrograph (SAMI) Galaxy Survey. We derived circular speed curves (CSCs) of gas and stars from non-parametric fits out to $r \sim 2r_{\rm e}$. For 12/14 with measured H I profiles, ionized gas and H I maximum velocities agreed. We fitted mass-follows-light models to 163 galaxies by approximating the radial light profile as nested, very flattened mass homeoids viewed as a Sérsic form. Fitting broad-band spectral energy distributions to Sloan Digital Sky Survey images gave median stellar mass/light 1.7 assuming a Kroupa initial mass function (IMF) versus 2.6 dynamically. Two-thirds of the dynamical mass/light measures were consistent with star+remnant IMFs. One-fifth required upscaled starlight to fit, hence comparable mass of unobserved baryons and/or DM distributed like starlight across the SAMI aperture that came to dominate motions as the starlight CSCs declined rapidly. The rest had mass distributed differently from light. Subtracting fits of Sérsic radial profiles to 13 VIKING Z-band images revealed residual weak bars. Near the bar major axis, we assessed $m = 2$ streaming velocities, and found deviations usually $<30\,\mathrm{km\,s^{-1}}$ from the CSC; three showed no deviation. Thus, asymmetries rarely influenced the CSC despite colocated shock-indicating, emission-line flux ratios in more than 2/3 of our sample.

Key words: galaxies: kinematics and dynamics – galaxies: spiral – galaxies: structure.

1 INTRODUCTION

Dark matter (DM) in disc galaxies has been probed both by detailed optical (e.g. Rubin et al. 1985) and H I studies (e.g. de Blok et al. 2008) of dozens of individuals, and in shallower

★E-mail: cecil@unc.edu

long-slit surveys of hundreds ranging over environment (e.g. Courteau 1997). These analyses show that possible non-circular motions, uncertain stellar M/L ($\Upsilon_\star$ hereafter), and diverse predictions of DM, make dynamical decomposition indeterminate (e.g. Dutton et al. 2005). In consequence, kinematical models over the optical extent of a galaxy are fitted equally well using priors ranging from almost all DM in diverse radial profiles (e.g. Noordermeer et al. 2007; de Blok et al. 2008) to minimal DM to a modified Newtonian dynamics (MOND; Milgrom 1983; McGaugh et al. 2010, and references therein). MOND matches many circular speed curves (CSCs) without DM just by upscaling baryonic (starlight+gas) M/L by separate but constant-with-radius factors for bulge and disc (Sanders 1996). Sometimes 'H I scaling' (e.g. Hoekstra, van Albada & Sancisi 2001) works: after fitting a 'maximal starlight disc', scaling the observed H I mass density places enough DM within the extended disc to fit the combined optical+H I CSC, and tightens (Pfenniger & Revaz 2005) the baryonic Tully–Fisher relation (McGaugh et al. 2000). The required scale factor decreases from $\sim 9 \times$ in luminous galaxies.

Now, multiheaded integral-field feeds to a spectrograph (e.g. Bland-Hawthorn et al. 2011) can map efficiently and uniformly the kinematics of warm plasma and starlight across thousands of galaxies in diverse environments to isolate components including bars. Mass densities mapped by these spectra accelerate well above the MOND critical value a_o/G with $a_o \sim 10^{-10}$ m s^{-2}, so Newtonian dynamics suffice. These uniform data sets allow coordinated estimation of the stellar population/formation history, starlight reddening, and both gas and stellar kinematics. Perhaps their powerful synergy, unfettered by a slit, can better constrain DM possibilities.

Therefore, this paper is a reconnaissance of 178 rotationally supported systems from the first quarter of the ongoing SAMI (Sydney-AAO Multi-object integral field spectrograph; Croom et al. 2012) Galaxy Survey (SGS, Bryant et al. 2014) of visible-light spectra across the central 15 arcsec diameters of ~ 3400 galaxies in diverse environments at $0.005 \leq z \leq 0.10$. A goal is to assess if SAMI spatial coverage and sampling can address DM content and bar induced motions, respectively, within $\sim 2 r_e$ of SGS galaxies. Although the SGS is an optical survey, so relatively dust sensitive, optical stellar populations are less controversial than those in rest-frame NIR surveys (e.g. Conroy 2013, and references therein). Schaefer et al. (2015) map radial variations of dust attenuation in the SGS; we assumed spatial averages. Incorporating this refinement will necessitate refitting GAMA Survey broad-band photometry, which is beyond our scope.

Section 2 explains how we mapped gas kinematics and derived masses. In Section 3, we report CSCs, and the resulting mass and M/L measured dynamically ($\Upsilon_\times$ hereafter), by enforcing consistency with exponentially declining star formation and plausible initial mass function – IMF ($\Upsilon_\star$ hereafter), and by fitting stellar population SEDs to *ugriz*-band photometry, (Υ_P hereafter). Section 4 discusses our results on disc and bar kinematics, and compares these Υs averaged over each galaxy. The inadequacy of photometric mass to account for the CSC revealed what non-stellar masses must do. Section 5 concludes.

2 METHODS

From the first ~ 830 targets observed in the SGS, we selected 344 rotationally supported galaxies having enough gas to map their CSC. We rejected eight whose inclination angle to us is too small ($i < 20°$) to be established reliably by photometry, and those very strongly barred or in obvious interactions. Next, we rejected those whose

CSC would be smeared excessively by our point spread function (PSF, Section 2.3.1), because of large inclination ($i > 71°$), compact size, or observed in atrocious conditions, leaving 163 GAMA Survey and 15 SGS 'cluster' subsample galaxies. Several dozen are in the public SGS Early Data Release (Allen et al. 2015) and span the full mass range of the SGS (Bryant et al. 2015); many more cluster discs will be reported in a paper in preparation. Fig. 1 shows examples. Fig. 2 and Tables 1 and 2 summarize their properties. Notable are compact bulges, evident as median *r*-band Sérsic shape parameter $n \sim 1.4$ (Fig. 2e). We mapped their CSCs using DISKFIT (Sellwood & Spekkens 2007; Sellwood & Zanmar-Sanchez 2010). For the GAMA Survey (Driver et al. 2011) subsample, we had GALFIT3 (Peng 2010) Sérsic radial profile fits to Sloan Digital Sky Survey (SDSS) bands (Kelvin et al. 2012) and VIKING *Z*-band (Lange et al. 2015) images (examples in Fig. 1). Subtracting this profile highlighted residual photometric asymmetries to investigate for kinematical disturbances; we estimated gas streaming in 13. We did not examine environmental influences (e.g. Amran et al. 1994) because barely 1/3 of the SGS had been observed at the time of writing.

2.1 SGS Observations and data processing

SAMI is comprised of 13 integral field units (IFUs) that are plugged into a custom field plate of 1° diameter on sky at the corrected prime focus of the 3.9-m aperture Australian Astronomical Telescope (AAT). Simultaneously, its 26 single fibres obtain the sky spectrum, while there coherent-fibre bundles direct images of field stars to the telescope guider CCD. Each IFU has 61 optical fibres each of core diameter 105 µm (1.6 arcsec on sky) and cladded diameter 115 µm (Bryant et al. 2015). The fibres in each bundle are arranged in four concentric rings that are fused together lightly to obtain 73 per cent fill factor over 14.9 arcsec diameter on sky. The fibres are then separated and routed to the AAOmega bench mounted spectrograph where light is split by a dichroic filter into blue and red beams thence through volume-phase-holographic gratings on to separate E2V CCD 2×4 K detectors. Blue spectra spanned $\lambda\lambda 370$–570 nm (i.e. covered the SDSS *g* band) at resolution $R = \Delta\lambda/\lambda \sim 1730$, red spectra spanned $\lambda\lambda 625$–735 nm at $R \sim 4500$ to approximate SDSS *r* band for the farther half of our sample.

Please refer to Bryant et al. (2015) for SGS target selection and observing procedures, and to Allen et al. (2015) and Sharp et al. (2014) for data processing. Median full width at half-maximum (FWHM) of our sample was 2.3 arcsec from Moffat function fits to simultaneously observed stars, providing ~ 40 independent spatial samples. Variance and covariance arrays were returned, the latter essential because SAMI spectra are correlated in 0.5 arcsec $\times$ 0.5 arcsec $\times$ 0.1 nm data cubes.

2.1.1 Emission-line processing

Calibrated cubes were then processed through the LZIFU code (Ho et al. 2014) to isolate and quantify the galaxy emission-line spectrum; we restrict our comments to further custom processing and analysis of its outputs. We corrected for Galactic attenuation using dust maps from Schlafly & Finkbeiner (2011), then corrected for an attenuating dust screen at the galaxy by assuming that the intrinsic Balmer decrement flux ratio away from an AGN is Hα/H$\beta = 2.86$ for case B recombination at 10^4 K and $n_e = 100$ cm^{-3}. Following Calzetti (2001), we obtained luminosity

$$L_{int}(\lambda) = L_{obs}(\lambda)10^{0.4A_\lambda} = L_{obs}(\lambda)10^{0.4k_\lambda E(B-V)_{stars}} \qquad (1)$$
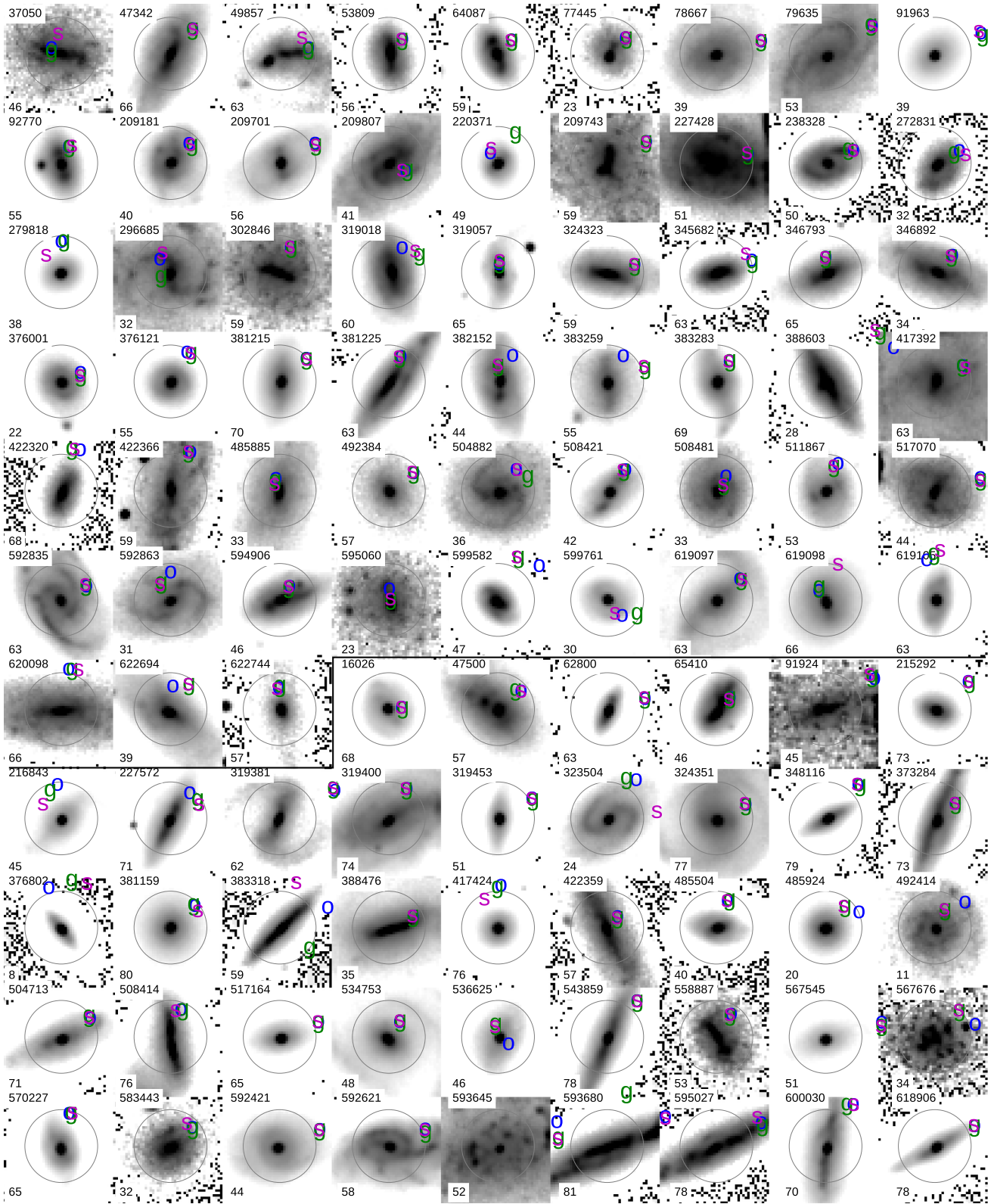
Figure 1. VISTA/VIKING survey Z-band log-intensity scaled images of some of our GAMA subsample, each 22 arcsec on a side with N at top, and having ~0.9 arcsec FWHM after deconvolution using PSF stars with 150 iterations of the Richardson–Lucy algorithm. SAMI coverage is encircled. Labelled at Sérsic r_e are major axis PA as blue 'o' for photometric, green 'g' for gas, and magenta 's' for stars. The galaxy ID is top left, and its inclination in degrees bottom left. Notable are the often very compact bulges. Those above the line are in our final sample, those below were rejected for various reasons including inclination outside our limits, a dominant bar that confounded a photometric inclination estimate, disorganized motions, or interaction.
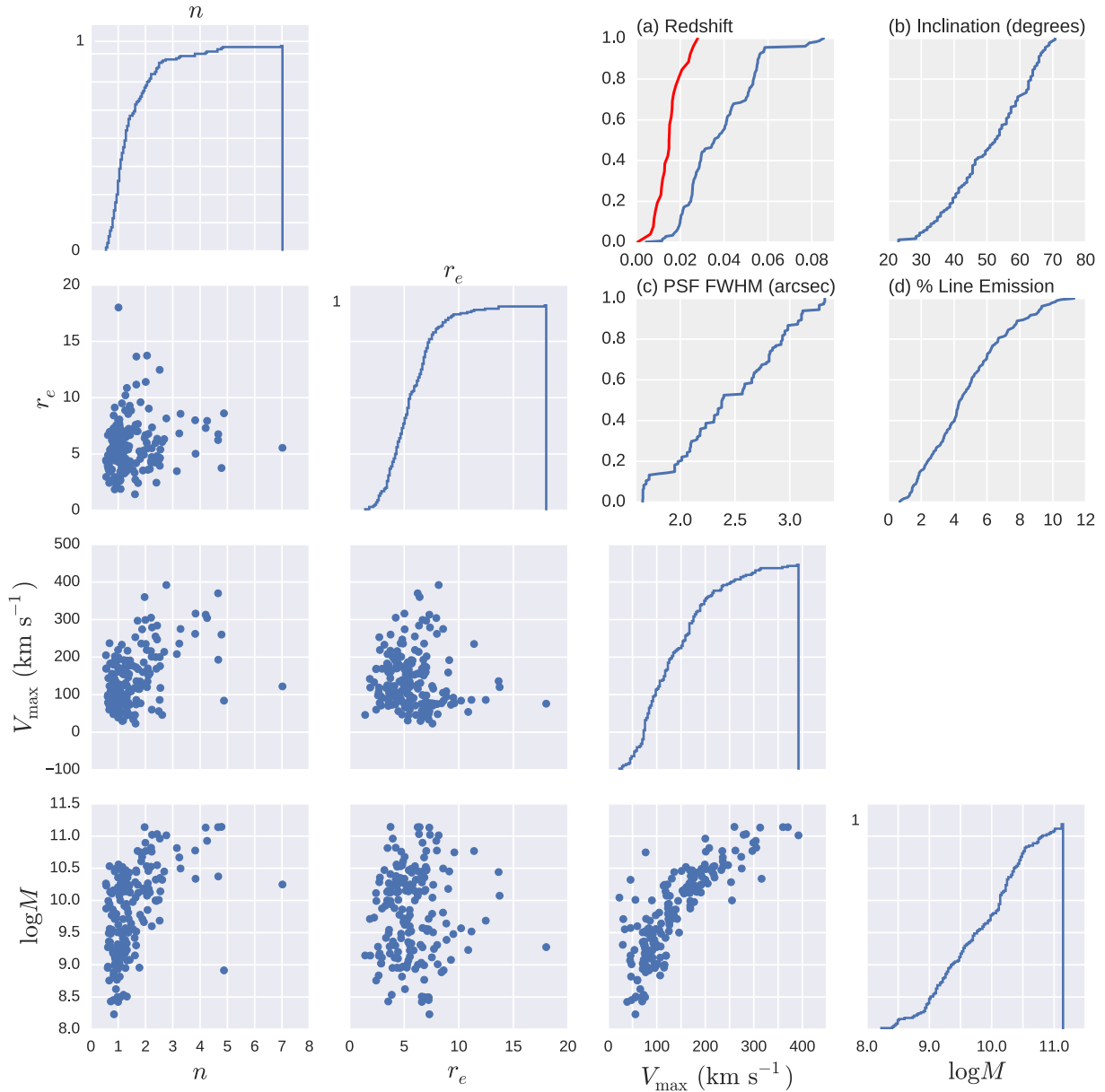
Figure 2. Properties of our GAMA subsample of 163 galaxies. Stellar mass estimates come from the GAMA catalogues, and are based on population synthesis fits to optical photometry (Taylor et al. 2011). r_e and n come from the single-component Sérsic fits of Kelvin (2013) to SDSS images. V_{max} comes from our CSC fits. In red in (a) are the generally smaller redshifts of the bar sample of Barrera-Ballesteros et al. (2014) from the CALIFA survey (Sánchez et al. 2012).

with the reddening curve band-averaged k_r = 1.16, $E(B − V)_{stars}$ = $0.44E(B − V)_{gas}$, and $E(B − V)_{gas}$ = $2.15\log_{10}[(H\alpha/H\beta)_{MWcorrected}/2.86]$.

Calzetti shows that this correction recovers the luminosity of star-bursting systems to a factor of 2 uncertainty, because internal dust is quickly destroyed in the burst to leave an idealized external screen. To bracket the effect of radial variations of dust, we first formed the decrement distribution from points with all but the faintest 5 per cent of the line-free R_CONTINUUM LZIFU image (approximating r band). Then, we biased the correction to significant starlight by using only line flux atop the brightest 40 per cent of that image; the medians of both of these distributions corrected the entire galaxy. A future paper will refit Sérsic profiles to multibroad-band photometry after radial corrections for dust attenuation and line emission.

2.1.2 Stellar velocity processing

Fogarty et al. (2014) detail SGS starlight processing. We considered only the blue data cube, $\lambda\lambda$370–570 nm at resolution $R = \Delta\lambda/\lambda \sim 1730$ to include most important stellar absorbers. A spectrum of high signal to noise (S/N) was made over 2 arcsec diameter centred on the galaxy, to which we fitted 985 MILES (Sánchez-Blázquez et al. 2006) stellar spectra using PPXF (Cappellari & Emsellem 2004) to adjust the coefficients up to fourth-order truncation of the Gauss-Hermite series. The best composite template was then readjusted with this polynomial to fit the line of sight velocity dispersion (LOSVD) of every spaxel in the data cube whose S/N > 5. In the blue data cube, this criterion is very close to S/N per Å. h_3 and h_4 almost always showed just noise for our sample galaxies.

Table 1. DISKFIT results for most of the SGS GAMA-Survey sub-sample. (3) Per cent of *r*-band flux from line emission. (4) ISM dispersion to normalize DISKFIT reduced χ^2 in (7). (5) Inclination is fixed at GAMA Survey SIGMA prior. (6) DISKFIT evaluated PA is east from N, bootstrapped error. (7) Reduced χ^2 of fit (degrees of freedom). (8) 1 = sharpest quartile, 2 = to median, etc. (9) Radius of maximum velocity within the SAMI aperture. (10) Dynamical $\Upsilon_\times$, broad-band colour fitted Υ_P corrected for line emission and dust. (11) Dynamical mass from (10).

GAMA ID (1)	z Fitted (2)	Line (per cent) (3)	ΔISM (km s^{-1}) (4)	Inclination (°) (5)	PA (°) (6)	χ^2 (DOF) Fit (7)	V_{max} (km s^{-1}) (8)	r_{max} (r_e) (9)	$\Upsilon_\times$, Υ_P (10)	$\Upsilon_\times \times L_r$ (10^9 M$_\odot$) (11)
8353	0.019623	9[b]	2.	50.9	162.3 ± 0.1	1.0 (161)	71 (3)	1.7	1.1, 1.5	2.9
15165	0.077651	1[c]	0.5	28.4	332.7 ± 0.1	0.6 (160)	392 (2)	1.2	4., 2.	115.6
15218	0.025612	5[b]	2.	56.6	324.7 ± 0.2	0.8 (149)	81 (1)	1.	2.9, 1.5	2.9
23117	0.081989	2[b]	1.	43.9	37.1 ± 0.3	1.4 (148)	315 (1)	1.	1.5[f], 1.9	118.4
23565	0.037239	2[b]	5.	56.6	30.6 ± 0.1	1.0 (153)	187 (3)	1.9	1.4, 1.9	23.9
30890	0.019945	5[b]	2.	55.9	289.3 ± 0.1	1.5 (177)	129 (1)	1.4	2.1, 1.7	8.2
32362	0.019052	2[a, e]	3.	55.9	315.7 ± 0.1	1.1 (186)	156 (1)	0.8	1.5[f], 1.9	27.7
37064	0.055355	2[d]	5.	42.3	126.1 ± 0.1	1.1 (187)	274 (2)	1.8	3., 1.8	47.4
41144	0.029712	5	3.	53.8	149.2 ± 0.6	1.1 (166)	190 (2)	1.3	1.6, 1.8	29.5
47342	0.024140	4	4.	66.4	334.7 ± 0.1	1.2 (138)	149 (1)	1.7	1.9, 1.9	10.6
49857	0.044137	10	4.	63.3	92.2 ± 0.1	1.0 (124)	74 (3)	2.3	2.1, 1.4	3.0
53977	0.048447	9[b]	3.	36.9	183.8 ± 0.2	1.2 (144)	123 (2)	2.	1.5, 1.5	15.7
55537	0.078761	2[b]	10.	63.9	359.4 ± 0.1	1.0 (93)	230 (3)	1.6	4.9, 1.8	31.4
55905	0.020973	6[c]	0.5	62.	192.1 ± 0.2	1.2 (116)	77 (1)	1.1	5.5, 1.5	1.5
56064	0.040377	2	5.	46.4	332.7 ± 0.4	1.0 (179)	169 (2)	1.3	1.3, 1.9	34.4
56183	0.039096	8[b]	3.	39.6	170.1 ± 0.1	1.2 (94)	80 (3)	1.7	1., 1.5	6.5
64087	0.055367	6[b]	7.	59.3	200.6 ± 0.1	0.9 (66)	229 (3)	2.2	1.9, 1.9	24.4
65278	0.042758	4[c]	0.5	69.5	44.9 ± 0.1	0.4 (66)	86 (2)	1.7	3.8, 1.6	2.0
65406	0.043096	2[b]	10.	31.8	96.3 ± 0.1	2.1 (172)	391 (1)	0.9	5.4, 2.	57.4
69653	0.018420	7[c]	4.	53.1	139.4 ± 0.3	1.0 (81)	57 (1)	0.9	3.5, 1.3	1.1
71382	0.021357	6[d]	1.	35.9	11.5 ± 0.1	1.1 (106)	94 (2)	1.5	3.6, 1.6	1.4
77754	0.053286	5[b]	4.	55.9	338.3 ± 0.1	1.1 (174)	209 (2)	1.5	2[f], 1.7	44.6
78667	0.055068	4[a, d]	2.	38.7	111.4 ± 0.1	0.9 (184)	168 (1)	1.5	3., 1.6	23.9
78921	0.02992	4[d]	2.	56.6	69.3 ± 0.1	1.1 (74)	95 (1)	0.7	6.3, 1.6	3.4
79635	0.040279	2[a, b]	3.	53.1	318.0 ± 0.1	1.0 (186)	207 (1)	1.2	3.8, 1.8	35.5
79771	0.042409	5[c]	0.5	45.6	346.5 ± 0.1	1.0 (122)	96 (3)	1.6	6.3[f], 1.4	1.7
84107	0.028829	10[b]	4.	39.6	186.6 ± 0.1	1.0 (183)	131 (1)	1.8	2., 1.4	9.5
84677	0.047392	7[b]	8.	62.6	334.5 ± 0.1	1.0 (127)	219 (2)	1.5	2.7, 1.8	41.2
85481	0.020062	3[c]	0.5	53.8	222.3 ± 0.1	0.9 (141)	97 (3)	2.1	2.3[f], 1.6	1.3
91963	0.050017	1[d]	1.	38.7	309.8 ± 0.1	0.9 (90)	293 (1)	0.8	3.8, 2.	66.8
99349	0.019791	4[b]	9.	67.7	52.4 ± 0.1	1.2 (112)	173 (1)	1.	2., 1.9	18.2
99393	0.020213	6[b]	2.	51.7	335.1 ± 1.4	1.4 (158)	127 (1)	1.8	1.2[f], 1.8	4.9
100162	0.025667	3[b]	4.	60.	232.8 ± 0.2	0.9 (64)	78 (3)	2.2	1.2, 1.6	2.5
100192	0.023994	8[b]	3.	23.1	44.7 ± 0.1	1.1 (109)	101 (1)	1.1	3.2, 1.6	3.7
105962	0.025503	6[b]	0.5	50.2	218.3 ± 0.1	0.8 (157)	77 (2)	1.5	2.3, 1.5	1.8
106042	0.026046	9	2.	36.9	95.1 ± 0.1	1.3 (105)	120 (1)	0.4	1.2, 1.5	30.8
106331	0.035938	7[b]	4.	55.9	157.8 ± 0.2	1.0 (152)	98 (1)	1.3	2.8, 1.5	7.0
106717	0.025704	10[e]	5.	45.6	109.5 ± 0.1	1.2 (139)	180 (1)	1.4	1.7, 1.6	20.6
137789	0.019103	4[c]	0.5	45.6	128.3 ± 0.8	0.5 (121)	116 (2)	2.5	5.3, 1.6	0.4
138066	0.035200	4[c]	0.5	53.8	270.2 ± 6.3	0.6 (163)	121 (3)	1.9	4., 1.8	3.2
143814	0.019880	12[b]	2.	67.	108.8 ± 0.2	1.8 (131)	79 (2)	1.6	1., 1.4	3.9
144402	0.035573	8[b]	10.	49.5	45.1 ± 0.2	1.9 (137)	192 (2)	1.8	1.6, 1.7	24.5
178481	0.025593	4[c]	2.	44.8	43.0 ± 0.1	1.2 (141)	63 (1)	0.9	1.5, 1.5	2.3
178578	0.019920	4	0.5	62.6	80.4 ± 0.3	0.6 (90)	37 (2)	1.1	2.3, 1.5	0.5
184281	0.019910	6[e]	0.5	64.5	179.2 ± 0.5	0.6 (102)	76 (2)	1.3	7.4, 1.5	0.7
184415	0.028315	6[e]	2.	40.5	88.5 ± 0.1	1.1 (139)	106 (3)	2.1	1.4, 1.6	5.6
185252	0.021583	9[c]	0.5	52.4	328.9 ± 0.8	0.4 (117)	58 (1)	1.	5.7[f], 1.5	0.7
185291	0.021649	7[c]	0.5	53.8	145.5 ± 0.7	1.0 (77)	47 (1)	1.2	1.7, 1.7	0.9
185532	0.020068	3[d]	0.5	28.4	76.1 ± 0.1	1.3 (157)	96 (1)	1.	6.1, 1.6	1.9
198591	0.011695	9	3.	48.7	240.6 ± 0.1	1.0 (167)	93 (1)	0.9	1.8, 1.7	3.8
198771	0.011690	4[b]	2.	70.7	98.1 ± 0.1	1.4 (98)	75 (1)	0.5	4., 1.4	4.8
204983	0.054962	1[b]	0.5	54.5	146.1 ± 0.1	0.8 (152)	255 (3)	1.9	2.9, 1.9	39.4
205097	0.055582	2[b]	0.5	57.3	273.3 ± 0.1	1.4 (135)	191 (3)	1.7	2.9, 1.9	21.7
209181	0.058250	8[b]	5.	39.6	324.6 ± 0.1	1.1 (197)	185 (2)	2.1	1.5, 1.5	33.8
209414	0.025713	5[c]	1.	56.6	6.1 ± 0.3	1.4 (135)	86 (1)	1.3	5.1, 1.6	1.6
209698	0.028588	5[e]	4.	59.3	312.4 ± 0.8	1.5 (55)	49 (2)	1.	0.1, 1.7	25.3
209701	0.053263	1[b]	3.	55.9	300.7 ± 1.0	0.9 (146)	297 (2)	1.3	5.2, 1.9	44.0
209743	0.040697	4[a, e]	10.	58.7	130.6 ± 0.1	1.1 (113)	173 (2)	1.1	3.2, 1.7	21.8

Table 1. – *continued*

GAMA ID (1)	z Fitted (2)	Line (per cent) (3)	ΔISM (km s^{-1}) (4)	Inclination (°) (5)	PA (°) (6)	χ^2 (DOF) Fit (7)	V_{max} (km s^{-1}) (8)	r_{max} (r_e) (9)	$\Upsilon_\times$, Υ_P (10)	$\Upsilon_\times \times L_r$ (10^9 M$_\odot$) (11)
209807	0.053893	4^b	5.	41.4	165.9 ± 0.1	1.3 (151)	209 (3)	2.2	0.8^f, 1.9	62.6
210660	0.016896	3^b	8.	57.3	143.8 ± 0.2	0.7 (113)	128 (2)	1.4	1.1^f, 1.8	8.1
210781	0.055356	2^e	1.	40.5	89.9 ± 23.	1.0 (148)	170 (2)	1.7	2.3, 1.8	21.3
216843	0.023886	$6^{a, b}$	4.	44.8	228.3 ± 0.1	1.1 (93)	76 (1)	0.8	4.1, 1.6	2.5
220332	0.020281	2^b	0.5	68.9	95.9 ± 0.1	0.5 (73)	89 (2)	1.	1.9, 1.9	3.6
220371	0.020275	4^e	1.	49.5	244.6 ± 0.1	1.3 (177)	91 (1)	1.5	2.3, 1.8	3.5
220439	0.019450	9^e	3.	34.9	20.1 ± 0.1	1.1 (187)	130 (2)	1.6	2.5, 1.6	4.7
220750	0.020993	5^e	0.5	45.6	311.1 ± 0.3	1.1 (87)	66 (2)	1.2	4.2, 1.5	0.8
221375	0.027765	6^b	3.	62.	40.1 ± 0.2	1.1 (129)	113 (1)	1.1	1.8, 1.6	11.1
227371	0.024828	6^e	0.5	65.8	255.6 ± 0.4	0.2 (139)	78 (2)	1.5	7.6, 1.5	0.7
227673	0.025838	7	3.	29.5	137.6 ± 0.1	1.1 (138)	90 (2)	1.6	2.6, 1.5	2.8
227970	0.054054	6^b	3.	40.5	204.3 ± 0.1	0.8 (156)	185 (2)	1.7	2.6, 1.6	24.7
238358	0.054220	4	10.	41.4	294.4 ± 0.1	2.2 (96)	285 (1)	0.8	2.9, 1.8	94.7
238395	0.024993	$9^{a, b}$	7.	34.9	67.4 ± 0.8	1.4 (162)	119 (3)	1.8	1^f, 1.6	10.0
239109	0.085402	1^d	2.	57.3	247.4 ± 0.1	1.5 (115)	361 (1)	1.2	4.2, 1.9	134.0
250277	0.058053	6^b	0.5	44.8	322.6 ± 0.9	1.1 (69)	56 (2)	1.3	0.4, 1.6	16.3
272667	0.022510	3^b	2.	43.1	268.0 ± 10.9	1.3 (183)	76 (1)	1.2	1.9, 1.7	3.9
273092	0.037521	4^e	0.5	41.4	64. ± 0.4	0.4 (145)	25 (1)	1.	0.1, 1.6	14.2
273296	0.020886	6^b	2.	57.3	348.9 ± 0.2	1.5 (141)	91 (1)	0.8	2.2, 1.5	6.8
273952	0.026862	6^c	0.5	48.7	341. ± 0.4	1.3 (127)	43 (1)	1.1	0.9, 1.6	2.7
278548	0.043219	4^e	5.	62.6	45.1 ± 0.5	1.2 (97)	113 (1)	1.	0.9, 1.7	22.6
278760	0.041235	9^b	2.	60.7	279. ± 0.1	1.1 (100)	137 (1)	1.6	2.6, 1.6	9.5
278812	0.041702	8^b	3.	65.8	223.6 ± 0.1	0.8 (87)	112 (1)	1.6	2.5, 1.5	6.4
279818	0.027289	$7^{a, b}$	2.	37.8	194. ± 0.3	1.4 (153)	44 (1)	1.	0.5, 1.6	4.
288461	0.004396	7^e	3.	53.8	223.5 ± 1.2	0.8 (149)	56 (1)	1.2	2.1, 1.3	0.3
296685	0.025415	3^e	0.5	31.8	126.8 ± 1.0	0.21 (101)	32 (2)	0.9	0.4, 1.7	2.7
296829	0.053763	2^b	5.	63.9	139.5 ± 0.3	1.08 (89)	167 (3)	2.1	2.1, 1.9	15.8
296847	0.025628	4^c	0.5	63.9	108.3 ± 0.1	1.1 (144)	90 (2)	1.4	4.7, 1.7	2.1
297633	0.055052	4	1.	41.4	353.4 ± 0.1	1.3 (152)	184 (1)	1.3	2.2, 1.7	40.3
300477	0.029288	7^b	1.	41.4	289.7 ± 0.1	1.0 (139)	100 (2)	1.4	3.7, 1.6	2.9
301346	0.04416	9^b	3.	57.3	71.5 ± 0.1	2.0 (117)	187 (2)	2.2	2.1, 1.7	18.2
301382	0.058449	11^b	5.	67.7	306.5 ± 0.1	1.4 (82)	108 (2)	1.9	1.2, 1.7	17.4
301799	0.051461	2^b	7.	67.	320.5 ± 0.2	1.1 (51)	168 (3)	2.	3.7, 1.9	7.3
303099	0.026026	1^b	5.	28.4	93.6 ± 0.3	1.3 (194)	338 (1)	1.8	6.4, 1.9	17.1
318936	0.017801	9^b	1.	50.9	209.3 ± 0.1	1.3 (123)	66 (2)	1.1	2.9, 1.4	1.4
319018	0.049157	5^b	7.	60.	131.4 ± 3.4	1.1 (96)	120 (3)	1.5	0.5^f, 1.7	15.2
319057	0.054817	8^b	7.	65.2	258.9 ± 0.1	1.1 (155)	196 (3)	2.3	3., 1.7	19.0
322910	0.031065	5^e	0.5	35.9	279.4 ± 0.8	0.5 (162)	36 (2)	1.4	0.1, 1.7	7.3
323507	0.039919	7^b	0.5	30.7	37.5 ± 0.1	0.8 (130)	155 (3)	2.2	3.4^f, 1.6	4.4
323855	0.040960	3^b	4.	37.8	261.7 ± 0.1	1.3 (187)	211 (1)	1.3	2.7, 1.8	42.5
323874	0.058114	5^c	0.5	23.1	307.1 ± 0.3	0.5 (100)	90 (3)	1.7	0.3, 1.5	34.0
325378	0.084761	1^b	0.5	53.1	117.6 ± 1.0	0.8 (65)	259 (2)	1.5	1.4^f, 1.9	74.5
345682	0.025492	3^b	1.	62.6	291.2 ± 0.2	1.62 (95)	84 (3)	1.8	1.4^f, 1.6	2.7
346793	0.056256	3^e	4.	65.2	67.3 ± 0.1	1.2 (121)	184 (1)	1.4	3.5, 1.7	26.3
346892	0.058541	$3^{a, e}$	2.	33.9	215.4 ± 0.4	1.3 (166)	171 (2)	2.1	2., 1.7	24.8
371789	0.026782	5^b	4.	52.4	4.3 ± 3.8	1.2 (115)	126 (3)	2.6	1.4, 1.9	6.7
376001	0.051317	1^b	0.5	21.6	85.8 ± 0.1	1.3 (109)	216 (3)	2.5	2.5, 1.9	18.9
376121	0.051593	1^b	10.	54.5	339.9 ± 0.2	1.5 (120)	287 (1)	1.2	2.1, 1.9	81.4
376185	0.034067	4^c	0.5	46.4	61.3 ± 0.1	1.1 (87)	71 (3)	2.1	1.2, 1.5	2.4
376340	0.050744	3^b	2.	63.9	199.8 ± 0.1	1.5 (97)	165 (3)	1.4	2.3, 1.7	23.8
376478	0.051322	3^b	3.	45.6	254.0 ± 0.1	1.6 (187)	171 (1)	1.3	3.7, 1.6	22.2
381215	0.050008	1	0.5	70.7	139.7 ± 0.4	0.8 (71)	187 (3)	1.3	6.7, 2.	12.6
381225	0.050369	3	6.	62.6	196.6 ± 0.1	0.9 (149)	180 (2)	2.	3., 1.8	20.7
382152	0.056768	2	2.	43.9	61.5 ± 0.1	1.3 (191)	135 (1)	1.9	1.8^f, 1.8	17.9
382631	0.054531	3	2.	32.9	145.9 ± 0.1	1.0 (106)	168 (3)	2.5	1.9, 1.8	16.9
383259	0.057246	1	4.	54.5	106.0 ± 0.1	1.0 (179)	94 (3)	2.	0.3, 1.8	40.8
383283	0.017288	4^a	1.	68.9	206.1 ± 0.1	1.1 (78)	90 (3)	1.7	2.3, 1.8	1.6
388451	0.012213	5	2.	70.1	49.4 ± 0.2	1.2 (117)	66 (2)	1.5	4.5, 1.5	0.5
418725	0.037778	4	4.	28.4	65.1 ± 0.1	1.5 (150)	271 (3)	2.8	2.9, 1.8	23.1
422320	0.031510	$6^{a, c}$	4.	67.7	175.6 ± 0.3	1.2 (112)	99 (1)	0.9	5., 1.5	5.1
422366	0.02867	$4^{a, d}$	3.	59.3	168.5 ± 0.1	1.0 (144)	109 (1)	1.	2.7, 1.6	7.9

Table 1. – *continued*

GAMA ID (1)	z Fitted (2)	Line (per cent) (3)	ΔISM (km s^{-1}) (4)	Inclination (°) (5)	PA (°) (6)	χ^2 (DOF) Fit (7)	V_{max} (km s^{-1}) (8)	r_{max} (r_e) (9)	$\Upsilon_\times, \Upsilon_P$ (10)	$\Upsilon_\times \times L_r$ (10^9 M$_\odot$) (11)
422619	0.028831	3^c	0.5	30.7	141.8 ± 0.2	0.5 (103)	89 (1)	0.8	3.1, 1.6	4.7
422761	0.076985	3	0.5	29.5	256.6 ± 0.1	0.5 (168)	194 (2)	1.7	2.3, 1.8	44.4
422933	0.029036	6^c	5.	65.8	199.3 ± 0.1	1.2 (137)	197 (2)	1.6	2.9, 2.	14.3
460374	0.025131	3	6.	46.4	25.6 ± 0.1	1.2 (184)	243 (1)	0.9	2.2, 1.9	60.7
485504	0.056051	2	0.5	39.6	26.7 ± 0.1	0.4 (151)	187 (2)	1.4	4.1, 1.8	18.8
485885	0.054931	3	1.	32.9	263.7 ± 0.1	1.4 (157)	169 (1)	1.5	2.9, 1.8	22.9
486872	0.042835	3^d	7.	54.5	122.0 ± 0.2	1.4 (164)	233 (1)	1.4	2.1, 1.8	37.6
487027	0.026325	10	8.	49.5	76.5 ± 0.2	1.1 (166)	156 (1)	1.4	2.9, 1.7	12.1
491552	0.024962	5	0.5	65.8	89.4 ± 11.0	1.1 (144)	98 (2)	1.6	4., 1.6	1.9
493621	0.029452	5	1.	39.6	260.2 ± 0.1	1.0 (151)	120 (2)	1.4	5.3^f, 1.5	2.0
504882	0.053942	2^b	2.	35.9	168.7 ± 0.1	0.8 (104)	162 (2)	1.6	2.7, 1.8	16.5
505788	0.042834	3^b	10.	45.6	149.3 ± 0.1	1.3 (158)	318 (1)	1.3	3.4, 1.9	72.5
505817	0.043804	5^c	1.	61.3	180.4 ± 0.2	1.4 (113)	121 (1)	1.7	8.2, 1.5	2.5
505979	0.043518	5^b	3.	63.3	143.1 ± 0.1	1.0 (154)	156 (2)	2.1	3.5^f, 1.6	8.5
508421	0.055285	2^e	1.	42.3	11.6 ± 0.1	1.7 (138)	216 (2)	2.	3.5, 1.9	22.7
508481	0.056138	3^e	2.	32.9	92.9 ± 0.1	1.1 (108)	144 (2)	1.6	2.8, 1.8	11.6
509444	0.03441	6^c	0.5	49.5	221.5 ± 0.2	0.4 (130)	76 (1)	1.5	5.6, 1.7	1.2
513066	0.029424	8^b	1.	67.	353.2 ± 0.2	1.6 (117)	75 (1)	1.	3.1, 1.4	4.3
517070	0.050899	4^b	3.	43.9	278.9 ± 0.1	1.3 (193)	156 (1)	1.8	2.6, 1.7	22.6
517164	0.049726	1^b	3.	64.5	278.0 ± 0.1	1.0 (116)	191 (2)	1.3	1.6^f, 1.9	29.4
517167	0.029883	6^b	1.	46.4	275.8 ± 0.1	1.3 (134)	108 (3)	2.	2.2, 1.6	3.6
517306	0.029578	7^b	2.	50.9	249.4 ± 0.2	1.3 (163)	102 (2)	2.2	1.7^f, 1.6	3.9
585359	0.035199	3^b	2.	63.9	176.4 ± 0.1	1.6 (153)	97 (2)	1.6	1.6, 1.9	20.4
585659	0.024858	4^c	1.	62.6	14.1 ± 0.2	1.5 (134)	97 (2)	1.8	4.3, 1.7	2.0
585755	0.040357	4^b	4.	68.3	91.6 ± 0.1	1.1 (121)	147 (2)	2.1	2.8, 1.7	8.2
592835	0.051664	5^b	8.	63.3	295.7 ± 0.1	1.2 (142)	197 (3)	2.5	1.8, 1.8	34.3
595060	0.044345	2^d	1.	23.1	297.7 ± 0.1	1.6 (194)	208 (3)	2.1	1.9, 1.8	28.7
599582	0.053112	2^b	0.5	47.2	355.0 ± 0.2	1.3 (181)	98 (1)	1.1	0.6, 1.8	45.5
599761	0.053421	1^b	3.	29.5	154.7 ± 0.1	1.3 (201)	298 (1)	1.3	3.9, 1.9	63.9
600026	0.050983	6^b	3.	43.9	302. ± 0.1	1.3 (146)	212 (1)	1.7	3.2, 1.7	21.6
610997	0.020496	6^b	4.	38.7	301.1 ± 0.3	0.8 (155)	110 (1)	1.4	3.7, 1.7	2.8
618116	0.050937	4^b	2.	43.1	276.4 ± 0.1	1.2 (186)	195 (2)	1.6	3., 1.6	27.9
618935	0.034336	6^b	2.	66.4	119.2 ± 0.1	1.1 (130)	158 (3)	2.3	1.9^f, 1.7	9.0
618992	0.054787	4	10.	64.5	343.3 ± 0.1	4.9 (59)	305 (3)	1.4	2.4, 1.9	63.5
619095	0.052577	5	3.	47.2	270. ± 0.1	1.4 (59)	320 (3)	2.8	2.2, 1.8	34.2
619098	0.035544	5^a	0.5	65.8	80.5 ± 0.1	1.0 (85)	80 (1)	0.9	3.1, 1.5	4.9
619105	0.025890	5$^{a, c}$	1.	63.3	213.5 ± 0.1	0.9 (151)	98 (1)	0.8	1.3^f, 1.6	10.4
620098	0.027918	7	1.	66.4	180.3 ± 0.1	1.3 (85)	95 (1)	0.9	3^f, 1.4	2.2
622429	0.040968	4^d	4.	58.7	135.1 ± 0.1	1.7 (136)	233 (2)	2.1	2.2, 2.	30.5
622434	0.041257	2^c	4.	51.7	182.0 ± 0.2	1.3 (183)	264 (1)	1.5	3.1, 1.9	36.2
622534	0.041263	4	0.5	68.9	300.8 ± 0.2	0.6 (95)	112 (2)	2.5	3.8^f, 1.6	2.4
622694	0.05245	3	3.	38.7	157.8 ± 0.1	1.17 (157)	205 (2)	1.6	1.2, 1.9	62.3
622744	0.013466	11^a	2.	57.3	221.8 ± 0.3	0.9 (173)	75 (2)	1.9	1.2^f, 1.5	1.9
623432	0.037998	5^d	4.	34.9	96.7 ± 0.1	1.3 (155)	302 (1)	0.9	3.6^f, 1.8	39.0

^{a}has H I velocity profile measurement (Fig. 8).
^{b}extended shock w/ asymmetric starlight.
^{c}extended shock, symmetric starlight.
^{d}compact shock at centre.
^{e}no shock but asymmetric starlight; otherwise no shock, symmetric starlight.
^{f}MXL fit failed because mass does not follow light. Changing the intrinsic flattening from $q = 0.1$ to $q = 0.05$ or 0.25 would multiply the listed $\Upsilon_\times$ by 0.76 or 1.3, respectively.

2.2 Surface photometry

We did not separate disc from bulge with different flattening and r-band Υ, but instead assumed that all starlight of constant $\Upsilon_\star$ is emitted by a flattened $q = 0.1$ homeoid of constant density within each nested shell. This is an approximation because disc light viewed as a Sérsic form varies on mass homeoids. A circular thick disc viewed at inclination i has ellipticity ϵ related to its intrinsic thickness q by

$$q^2 = \frac{(1 - \epsilon)^2 - \cos^2 i}{1 - \cos^2 i}. \tag{2}$$

Table 2. DISKFIT results for the SGS cluster subsample.

GAMA ID (1)	z Fitted (2)	ΔISM (km s^{-1}) (3)	Inclination (°) (4)	PA (°) (5)	χ^2 (DOF) Fitted (6)	V_{max} (km s^{-1}) (7)
011327.21+000908.9	0.043 193	2.0	45.7 ± 11.7	−28.2 ± 4.4	0.88 (163)	142
011415.78+004555.2	0.042 379	4.0	40.1 ± 9.8	47.9 ± 1.5	0.99 (160)	173
011456.26+000750.4	0.041 427	4.0	39.8 ± 11.3	−75.9 ± 2.3	1.26 (165)	287
215604.08−071938.1	0.057 945	4.0	38.5 ± 5.7	26.7 ± 0.6	0.80 (176)	267
215636.04−065225.6	0.064 572	2.0	51.8 ± 1.8	−10.3 ± 0.6	0.93 (172)	197
215826.28−072154.0	0.060 626	1.0	22.6 ± 5.6	58.6 ± 0.7	0.77 (145)	305
011346.32+001820.6	0.044 146	4.0	68.3 ± 6.9	−85.1 ± 0.8	0.91 (189)	292
215432.20−070924.1	0.059 227	5.0	25.1 ± 18.0	61.0 ± 2.8	1.06 (108)	511
004130.29−091545.8	0.044 808	5.0	42.9 ± 5.8	−1.2 ± 1.6	0.94 (154)	256
215705.29−071411.2	0.060 225	1.5	35.8 ± 8.6	−12.5 ± 0.8	1.18 (142)	237
215743.17−072347.5	0.056 766	3.0	35.2 ± 10.4	−33.6 ± 2.5	1.04 (148)	332
215759.85−072749.5	0.057 98	1.0	26.3 ± 7.2	27.7 ± 1.5	0.82 (137)	250
215853.98−071531.8	0.052 52	5.0	58.7 ± 4.8	−5.3 ± 2.1	0.92 (138)	242
215910.35−080431.2	0.052 561	4.0	40.9 ± 7.1	−48.5 ± 1.5	1.20 (171)	261
215924.41−073442.7	0.058 004	2.0	30.1 ± 8.9	−39.4 ± 1.5	1.23 (143)	254

(3) ISM dispersion to normalize DISKFIT reduced χ^2.
(5) DISKFIT evaluated PA is east from N, bootstrapped error.
(6) Fit (degrees of freedom).

Table 3. DISKFIT results for some plausible weak bars.

GAMA ID (1)	z Fitted (2)	ΔISM (km s^{-1}) (3)	Inclination (°) (4)	Disc PA (°) (5)	χ^2 (DOF) Fit (6)	Bar PA (°) (7)	$V_{\text{t, max}}(r/r_e)$ (km s^{-1}) (8)	$V_{\text{t2, max}}$ (km s^{-1}) (9)	$V_{\text{r2, max}}$ (km s^{-1}) (10)
79635	0.04033	6	53.1	−42.7 ± 0.9	1.0 (192)	−73	209 (1.3)	11	7
209807	0.05386	10	41.4	−187.5 ± 1.4	1.1 (177)	−164	216 (3)	41	30
279818	0.02724	3	37.8	197.5 ± 1.9	1.2 (177)	164	35 (>1)	3	3
319018	0.04897	10	60.0	136.2 ± 4.8	1.7 (120)	190	130 (2)	16	24
376121	0.05166	10	54.5	−19.4 ± 1.3	1.9 (72)	−7	282 (6)	23	51
383259	0.05715	5	54.5	110.1 ± 2.0	1.1 (146)	170	77 (1.1)	10	19
485885	0.05492	4	32.2	261.4 ± 0.6	0.9 (144)	278	168 (1.1)	27	20
508421	0.05524	10	42.3	11.2 ± 1.1	2.8 (136)	347	225 (1.5)	13	10
517070	0.05086	5	43.9	−80.6 ± 0.8	1.1 (178)	−61	164 (1.5)	13	10
595060	0.04432	2	23.1	295.2 ± 0.9	1.2 (189)	241	204 (2.4)	20	35
599582	0.05307	4	47.2	−6.3 ± 2.9	1.0 (158)	69	101 (1)	17	19
599761	0.05333	6	29.5	−205.7 ± 0.3	1.0 (194)	−150	302 (1.1)	22	31
619095	0.05250	10	47.2	−88.2 ± 0.6	1.0 (167)	−146	234 (2)	29	11

(8) CSC maximum velocity in SAMI aperture at the r/r_e shown.
(9) Tangential $m = 2$ motion.
(10) Radial $m = 2$ motion.

We used $q = 0.1$, but q from 0.05 to 0.25 produced comparable CSC shapes but with amplitude altered by < 15 per cent (Noordermeer 2008) and multiplied $\Upsilon_\times$ values in Table 1 column (10) by 0.76 and 1.3, respectively. $q = 0.25$ is appropriate for a dominant 'bulge', which Fig. 2 shows is rare in our sample and confirmed by the few with Sersic shape parameter $n > 2.5$. The SIGMA (Structural Investigation of Galaxies via Model Analysis) script of Kelvin et al. (2012) calls SOURCE EXTRACTOR (Bertin & Arnouts 1996), PSF EXTRACTOR (Bertin 2013), and GALFIT3 to fit a radial flux profile with the Sérsic function of index n, shape $b_n = 1.9992n − 0.3271$, of surface brightness Σ_e at effective radius r_e. SIGMA returns the surface brightness in mag arcsec^{-2} μ_e at r_e, $I_o(n) = e^{b_n} 10^{0.4(21.572+M_{r\odot} −\mu_e)}$, and the apparent magnitude extrapolated from a few r_e out to $10r_e$ $\equiv m_{10\text{re}}$ (often ~30 mag arcsec^{-2}). From the last, galaxy abso-

lute magnitude is $M_r = m_{r, 10re} − (5\log_{10}D_L + 25 + K_r + A_r)$ for K-correction $K_r = 1.2z$ (Kelvin 2013) to $z = 0$, dust absorption A_r, and D_L the luminosity distance in Mpc. Although some of these quantities are covariant, we had only their uncertainties. We converted to solar luminosities by assuming that solar absolute magnitude in r band $M_{r\odot} = 4.67$. We subtracted LZIFU-derived fluxes of relevant emission lines for each galaxy from $m_{10\text{re}}$. This line-emission correction and our dust correction A_r both used median values over the 40 per cent brightest r-band continuum.

To compare to dynamical masses, we fitted broad-band SED templates across the *ugriz*-band images from the SDSS DR9; please consult Taylor et al. (2011) for details on Bayesian procedures and priors also used here. These fits mapped stellar mass, optical-band

starlight weighted ages, and photometric M/L across our sample galaxies; all these assume solar metallicity. Comparing radial patterns of dynamical versus stellar mass and age is beyond our scope, so in Section 3.4 we just use values averaged over the brightest 40 per cent of the *r*-band starlight of each galaxy. Hereafter, we denote the averaged M/L derived thus as Υ_P.

As outlined in Section 2.5, to explore streaming motions we examined the residual images formed by subtracting the single-Sérsic fits from SDSS *r*-band and VIKING Z-band images.

2.3 Fitting disc velocities

We now describe how we extracted CSCs by fitting observed gas motions to a disc that approximated the flattened mass homeoid. Non-circular motions can appear in either a warped disc (an inclination ϕ-warp or in-plane PA-warp) or flat disc with $m > 0$ modal velocity distortions (Staveley-Smith et al. 1990). DISKFIT handles such motions independently but not in combination. We first discuss the assumptions of this code, how it accounted for beam smearing, and its use to map rotational and streaming motions within a galaxy.

2.3.1 Assumptions

DISKFIT fits radial variations of line-of-sight emission-line velocities across a disc all at once with common centre; it does not parametrize velocities over radius and does not require any asymmetries to be weak. It is a kinematical, not hydrodynamical, code so does not address bar or spiral-arm shocks. DISKFIT bootstraps uncertainties of its model velocities at each spaxel by scrambling fit residuals around each elliptical ring, then adding those to the original data and refitting (see the above references for details); we used 800 resamples at each radius, running these in parallel after updating DISKFIT to use modern Fortran coarrays for multicore efficiency.

Each fitted spaxel *n* has associated uncertainty σ_n, complicated for SAMI by high spatial covariance with neighbours (Sharp et al. 2014, discuss this covariance). Covariance is specific to each plug plate of 12 galaxies from seeing variations during the seven constitutive exposures. LZIFU reports the variance of its parameter estimates and handles spectral covariance between its multiple velocity components. To reduce covariance, we rebinned spectra into $2 \times 2 = 1$ arcsec^2 spaxels and used Monte Carlo methods to propagate spatial covariance and variances to a CSC. To ensure statistical independence in $\sim$2 arcsec FWHM seeing we should have told DISKFIT to 'stride' across the velocity map at every 2 binned pixels. However, that would have led to <5 independent spaxels from too many elliptical rings, too few for a reliable χ^2 contribution (equation 4). We therefore sampled at 1 arcsec.

'Beam smearing' can blur velocity gradients to distort the inner rise of the CSC (e.g. Sofue et al. 1999) where stellar bars may influence velocities and secular evolution (Kormendy & Kennicutt 2004). It manifests as a broad uncertainty on each CSC point from light smeared into the fitting ellipse; the defect increases with galaxy inclination.

To assess its impact, we used the CSC parametrization of Catinella et al. (2006) in terms of galaxy M_I and R_{opt} (83 per cent of the *R* band light is encircled on sky). We approximated the former from the GALFIT3 of Kelvin et al. (2012) to the SDSS *r*-band images (FWHM $\lesssim$ 1.5 arcsec), adjusted by $(r - i) = 0.40 \pm 0.05$ dex (originally from Blanton et al. 2003, revised by Kelvin et al. 2012) appropriate for blue-sequence galaxies. Replacing the latter, we formed a more sensitive metric of smear by first taking the median of the *r*-band Sérsic r_e as projected around the ellipse. We then

divided that into the half-width at half-maximum of the Moffat-function fit to the contemporaneous SAMI PSF to rank the sample from least to most blurred, see column (8) of Table 1. Panels (b)–(d) of Fig. 3 show, for the M_I from the GALFIT3 to each galaxy, the Catinella et al. (2006) parametrization smeared with various quartile seeing. The linear rise of CSC of more massive galaxies ($v_{max} > 200$ km s^{-1}) was undistorted only in the sharpest quartile; for less massive ones, up to median blur was acceptable.

To de-smear, DISKFIT smoothes the fit model by adjusting the fractional contribution of the nearest 11 spaxels to a spaxel in the nominal fitting ellipse. This tactic succeeds only when the CSC is sampled less often than twice the seeing FWHM. For most of our data cubes this would require >4 arcsec sampling, hence leaving only 1–2 points plus v_{sys} to trace the CSC. Instead, we explored the effectiveness of partial correction by tracking how CSC points and their uncertainties adjusted as smear correction progressed – and perhaps converged – from 0 to 0.75 arcsec to 1 arcsec FWHM. We found that most bootstrap uncertainties shrank considerably with only 0.75 arcsec FWHM correction, to deliver an informative CSC at 1.5 arcsec increments. The corrected distribution at each radius was centred in the upper half of the original distribution, as expected.

The LZIFU multi-Gaussian parametrization of each spectrum accounts for stellar absorption that might shift the velocity centroid of line emission. We fitted to gas velocities only within an ellipse centred on the nucleus whose major axis extent and PA was set by the Hα map, and whose minor axis extent was just the projected major axis extent. We omitted nearly face-on or highly inclined galaxies, considering only $20° < i < 71°$. We generally fixed inclination to that derived by SOURCE EXTRACTOR from the SDSS *r*-band image (see Section 2.2); the SIGMA code did not output SOURCE EXTRACTOR inclination uncertainties, so we assumed 5 per cent of the mean for its σ. A warped or non-circular disc will give a bad prior inclination, most strongly influencing the CSC of near-face-on modelled plane discs. Inclination warps seem to be rare for optical discs, but often start beyond in H I (Sancisi 1976). PA-twists are less well studied but more common due to bar/oval streaming. We found that DISKFIT was unreliable on PA-twisted discs, so these were rejected when we defined our sample.

We fitted two sets of velocities: (1) just the one-Gaussian model of LZIFU, which is robust but can miss flux in the wings of emission-line profiles; (2) full non-Gaussian profiles obtained by synthesizing the Hα emission-line profile from all LZIFU components. We mapped uncertainties for (2) by random sampling the LZIFU Gaussian uncertainty distributions of the fitted multicomponent velocities and their dispersions, Hα fluxes, and various estimates of the Balmer α absorption correction provided by different spectral templates, each time recomputing the flux weighted median velocity. The median of the resulting distribution of medians was the adopted velocity at that spaxel, and its $\pm$34 per cent spread averaged around median was our error weight for the CSC fit. Our fits ignored outliers in the deprojected ellipse that deviated by >50 km s^{-1} from neighbours.

We fitted two models with smear correction 0.75 arcsec FWHM: (1) for the GAMA subsample with its photometric Gaussian prior on inclination, allow the PA to vary; (2) also vary inclination from the GALFIT3 model estimate (Kelvin et al. 2012) of the Sérsic profile; the centre was always allowed to vary by $\pm$0.5 arcsec from its photometric prior value. We found that the second tactic never improved the fit. Galaxies in our SGS 'cluster' subsample lacked GAMA priors, so fits always varied disc inclination and PA. This extra freedom increased variance of the CSC fit, so we imposed coincident kinematic and photometric centres to stabilize those fits.
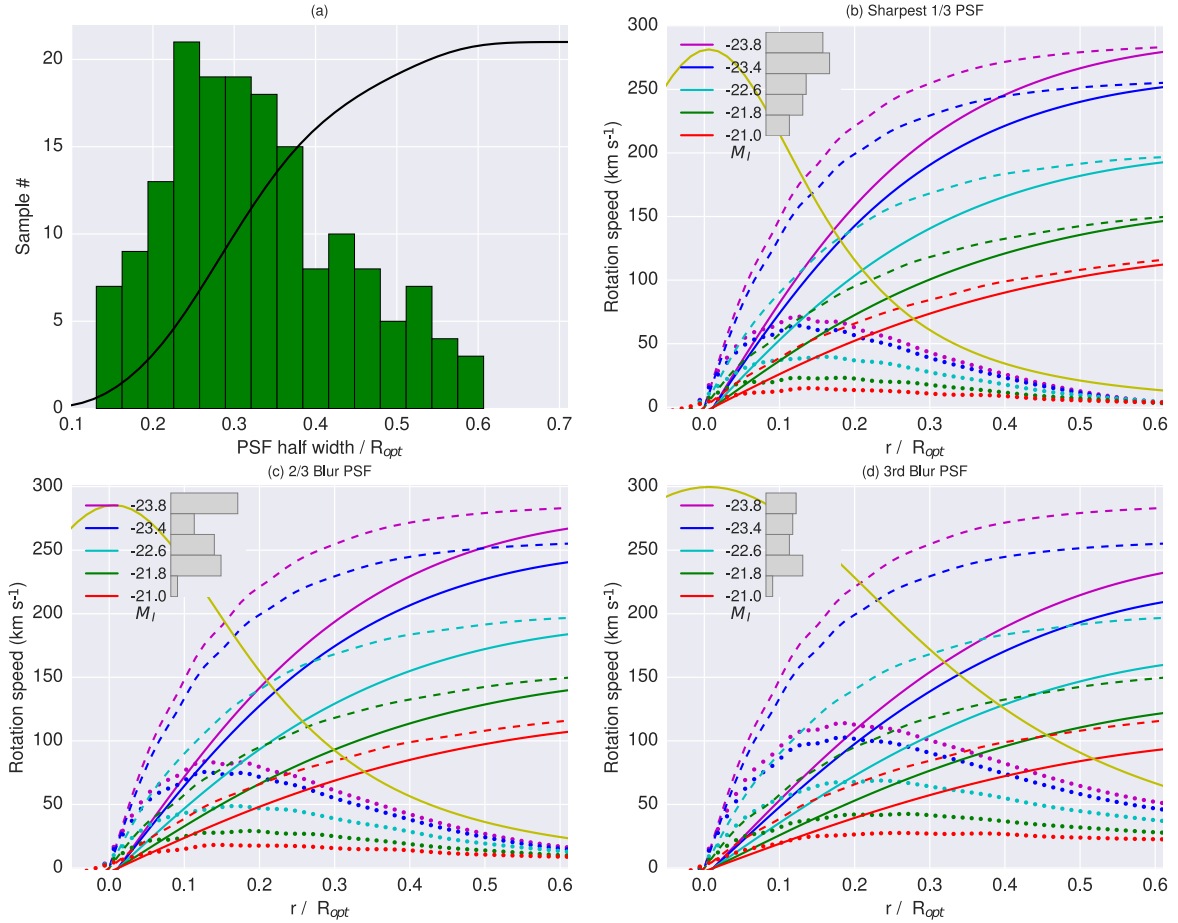
Figure 3. How the SAMI PSF smears inner CSCs for our mass range. (a) Distribution of (Moffat-function PSF Half-Width)/R_{opt}. (b)–(d): dashed are the Catinella, Giovanelli & Haynes (2006) parametrization of disc only CSCs for the galaxy absolute magnitude bins M_I shown with curves plotted from largest to smallest. Solid lines: after convolving these with the PSF in yellow at the quartile boundary. Dotted: differences. The grey histograms show the relative number of sample galaxies in each M_r bin, approximating M_I as described in the text.

SIGMA fits of the full SGS 'cluster' subsample are underway, a paper in preparation will present their CSCs and mass models.

Ho et al. (2014) demonstrate that LZIFU maps emission lines whose flux ratios diagnose shock velocities and the shock fraction of the total shock+photoionized emission. Shock models are parametrized by the ionization of pre-shocked gas, shock velocity, and magnetic pressure. We used the MAPPINGS3 code (Sutherland & Dopita 2003) inputs of Ho et al. (2014) that were bounded for the SGS by combining [O III]/Hβ with [S II]/Hα or [N II]/Hα shock diagnostics; these choices ranged over the ratios evident in our sample. By correlating the shock maps with $m = 2$ residuals in velocity field, we assessed if shock velocities were consistent with kinematical deviations. We did not tune model pre-shock ionization or magnetic pressure.

2.3.2 Axisymmetric fits

For these, $V_{2,t}(r) = V_{2,r}(r) = 0 \ \forall \ r$. Fig. 4 shows the displacements between rotational and photometric centres. As mentioned, for the GAMA subsample, we fixed i to the value derived from the single-Sérsic GALFIT3 to SDSS r-band photometry (Kelvin et al. 2012).
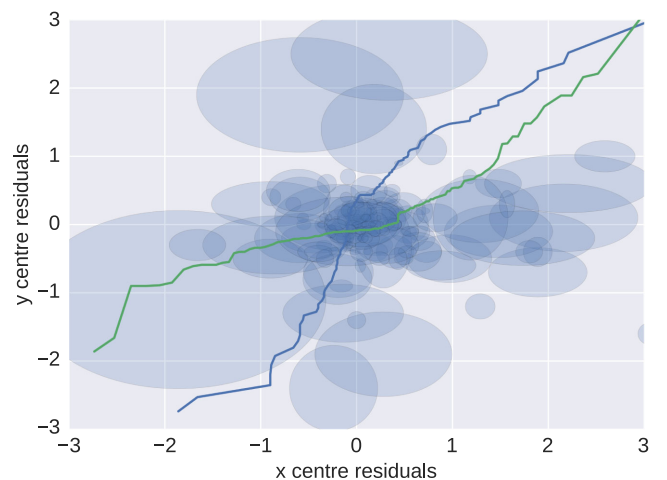
Figure 4. Difference between some photometric nominal and fitted kinematical disc centres; unit is 0.5 arcsec pixel and uncertainties are $\pm 1\sigma$. The cumulative histograms of the differences are also shown, starting from the lower-left corner.

2.3.3 Fitting procedure

To derive $V_t(r)$, $V_{2,t}(r)$, $V_{2,r}(r)$, ϕ_b, V_{sys}, i, and PA θ from the major axis, DISKFIT fits observed gas velocities to

$$V_{model} = V_{sys} + [V_t(r)\cos\theta - V_{2,t}(r)\cos m(\theta - \phi_b)\cos\theta$$
$$- V_{2,r}(r)\sin m(\theta - \phi_b)\sin\theta]\sin i. \quad (3)$$

At N sky positions (x, y), it minimizes

$$\chi^2 = \sum_{n=1}^{N} \left(\frac{V_{obs}(x, y) - \sum_{k=1}^{N} w_{k,n} V_k}{\sigma_n} \right). \quad (4)$$

Velocity uncertainties are taken uncorrelated of form $\sigma_n(x, y) = \sqrt{\Delta_D(x, y)^2 + \Delta_{ISM}^2}$ with Δ_D our estimated velocity uncertainty described above. Δ_{ISM} is 'ISM turbulence', increased ad hoc from 0 until the reduced χ^2 was approximately normalized; see Tables 1 and 2. See Sellwood & Spekkens (2007), Sellwood & Zanmar-Sanchez (2010), and the code documentation for details. One anticipates more dispersion near strong bars, e.g. $\sigma_{z,bar} \sim 30\,km\,s^{-1}$ for young bars and $\sim100\,km\,s^{-1}$ for evolved ones (Gadotti & de Souza 2005), but we had excluded atypical, strong photometric bars a priori.

2.3.4 Non-axisymmetric fits to streaming motions

After beam correction, inner points whose velocities deviated from the photometrically motivated CSC suggested the need to evaluate non-circular/decentred motions. Such affect CSC values and uncertainties even beyond the distortion because the galaxy centre is adjusted to minimize fit residuals across the disc. Consistent deviation across several rings is needed for reliability, hindering application of DISKFIT to SAMI data cubes with their at most 50 independent spatial points.

For 13 galaxies, velocity residuals never shrank after adding to the model an $m = 2$ asymmetry whose fixed major axis PA extended slightly beyond the photometric single-Sérsic-fit residual. To these we first fitted with a variable bar PA, then explored how χ^2 varied at fixed bar PAs adjacent to the optimal value. If χ^2 changed negligibly, we simply aligned kinematical and photometric bars. $m = 0$ and 2 components are degenerate, hence fits are unreliable, when the two PAs differ by $\sim0°$ or $\sim90°$. Using an $m = 1$ mode likewise did not shrink fit residuals. The appendix discusses the non-axisymmetric systems, among others.

2.4 Estimating dynamical M/L and mass

CSCs across the optical extent of galaxies can often be fitted with variable $\Upsilon(r)$ (VML; e.g. Takamiya & Sofue 2000), reaching $\lesssim10\Upsilon_\star$. To explore the mass distribution that drives the CSC, we used SDSS DR9 r-band images because of reduced S/N and uncertain $\Upsilon_\star$ at longer wavelengths. We sought the fraction of a CSC due to stars to assess as yet unobserved baryons and, ultimately, DM by any deficit between model and data. We denote by $\Upsilon_\times$ the maximum fitted value unconstrained by IMF considerations. It merely scaled starlight to CSC by asserting constant Υ_r (CML hereafter) to see how much DM might be distributed like starlight. The few fits that still failed must have VML if their values were $\sim\Upsilon_\star$, or mass that does not follow light.

We integrated numerically the mass density contributed at each radius from the fit to the Sérsic profile

$$I_S(x) = I_o(n) \exp[-(\frac{x}{r_o})^{1/n}] \quad (5)$$

to obtain the $CSC(r)^2$

$$V^2(r) = C \int_0^r \frac{m^2 dm}{\sqrt{r^2 - m^2\varepsilon^2}} \int_m^\infty \Upsilon_r(x)(\frac{x}{r_o})^{1/n-1}\frac{e^{-(x/r_o)^{1/n}}dx}{\sqrt{x^2 - m^2}} \quad (6)$$

with $C = \frac{4Gq I_o}{r_o n}\sqrt{\sin^2 i + \cos^2 i/q^2}$ (Noordermeer 2008). We used either CML $\Upsilon(r) = 1$ or VML

$$\Upsilon(r) = \Upsilon_{r,1} \exp\left[-\alpha(s)\left\{\left(\frac{r}{r_e}\right)^s - 1\right\}\right]. \quad (7)$$

Monte Carlo methods propagated uncertainty distributions of assumed A_r, and the LZIFU velocity and line-emission luminosity corrections, to the CSC. These uncorrelated errors weighted the linear least-squares fit (MATHEMATICA V10 LINEARMODELFIT) to bound Υ uncertainties.

2.5 Bar photometric asymmetries

The VIKING (VISTA Kilo-degree Infrared Galaxy Survey; Lawrence et al. 2007) Z-band image (Fig. 1) sometimes motivated a dual-Sérsic decomposition (Lange et al., in preparation): a pair of quite different n, PAs, and r_e.

We interpolated the 'disc' inwards and subtracted it to isolate bulge/bar starlight that we then parametrized with the second Sérsic profile. Because central features are compact (Fig. 1), the resulting 'discs' have mass distributions close to those derived from the single-Sérsic fits. We deprojected each image to face-on with the GALFIT3 orientation, rebinned the result into five 1 arcsec wide radial bins and 32 11°25 wide angular bins, then Fourier transformed each angular set and formed the power spectrum up to $m = 4$. Unfortunately, compact features prevented quantification of bar strength by Gaussian fitting the radial extent of their modes (Buta et al. 2006; Buta, Corwin & Odewahn 2007).

2.6 Spatially integrated H I velocity profiles

H I content of several dozen rotationally supported SGS galaxies came from either the Arecibo Legacy Fast ALFA (ALFALFA; Giovanelli et al. 2005) survey or early observations from a dedicated follow-up of SGS targets, as described below.

ALFALFA is an H I-blind survey using the ALFA multibeam receiver at Arecibo to cover 7000 degrees squared of sky at resolution 3.5 arcmin and $5\,km\,s^{-1}$, and should detect $>30\,000$ galaxies to $z \lesssim 0.06$. Arecibo observations are limited to $-1° < \delta < 37°$, so ALFALFA covers only part of the equatorial GAMA fields. Furthermore, the current ALFALFA data release (Haynes et al. 2011) is limited to declinations $>4°$, so the H I spectra presented in Section 3.2 were kindly provided by the ALFALFA team before publication. H I masses will be published by the ALFALFA team, but our detections were substantially smaller than $L_r \times \Upsilon_\star$ discussed in Section 4.3. Molecular mass should be even smaller.

An ongoing Arecibo programme targets SGS galaxies in equatorial GAMA fields that ALFALFA did not detect and uses the L-band wide receiver plus same correlator setup as the *GALEX* Arecibo SDSS Survey (GASS; Catinella et al. 2010, 2013). Spectra are processed with GASS software, and velocity widths are measured at the half height of each peak using the technique adopted by GASS and ALFALFA. These deeper spectra were available for six of our sample galaxies. Unfortunately, radio-frequency interference from the San Juan International Airport radar is preventing study of many SGS discs near $z \sim 0.05$.
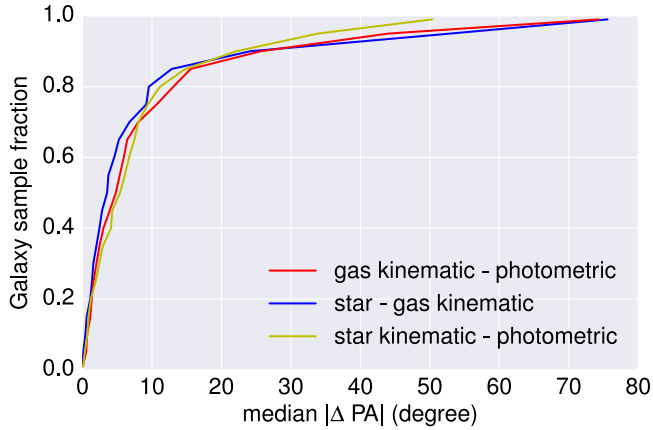
Figure 5. Distributions of absolute differences between photometric and the two kinematically established PAs for our SGS GAMA subsample. Plotted is the mean value within the SAMI aperture. PPXF fitted stars, DISKFIT gas, and SIGMA the photometry.

3 EMPIRICAL RESULTS

3.1 Stellar/gaseous velocities and PAs compared

To assess disc orbit regularity and flatness within the SAMI aperture, following Verheigen & Sancisi (2001) we plotted the kinematical line of nodes (LON) for both rotational stellar and gaseous velocities, then traced maximum velocity found within each elliptical ring. A flat, axisymmetric disc has straight photometric LON. A disc with slightly elliptical stellar orbits will show systematic differences in PA between photometric and kinematic LONs where orbits crowd. A twisted, antisymmetric LON across the nucleus indicates a strong bar or oval distortion. Fig. 5 summarizes such distortions across our GAMA subsample, plotting cumulative distributions of angular differences between gaseous, stellar, and photometrically derived PAs; Fig. 6 shows an example. Stellar versus photometric values deviate by $>25°$ for 20 per cent. Fig. 7 compares the central stellar LOSVD to the peak gas CSC. Within a substantial bulge, asymmetric drift will reduce LOSVD below the CSC. Almost all trend this way despite small bulges: the CSC peak almost always exceeded stellar σ averaged over r_e by $\sim 120 \, \mathrm{km \, s^{-1}}$.

3.2 Circular speed curves

Tables 1 and 2 include the observed peak value v_{max} at radius r_{max} from our CSC fits. Fig. 8 compares the peak value of our CSCs with the H I velocity extent $W50/2 + 2\sigma$; almost all CSCs attain at least 90 per cent of the H I amplitude. Indicated too is the asymmetry of the H I profile, measured as the ratio of integrated blueshifted/redshifted flux. Despite ± 20 per cent variations in this, we found no trend in CSC residuals that would arise from $m = 1$ mass asymmetries. Fig. 9 shows the CSC and 2σ uncertainty spread at each radius. Some beam-smear corrected CSCs rose gradually across the SAMI radius, maximizing near the Sérsic r_e in Table 1 column (9). We discuss the Fig. 9 fits in Section 4.3.

3.3 Mass estimates

Column (10) of Table 1 reports Υ_P (1.7 median) from fits to the *ugriz*-starlight defined SED of the GAMA subsample. These revealed that the starlight weighted ages are Gaussian distributed
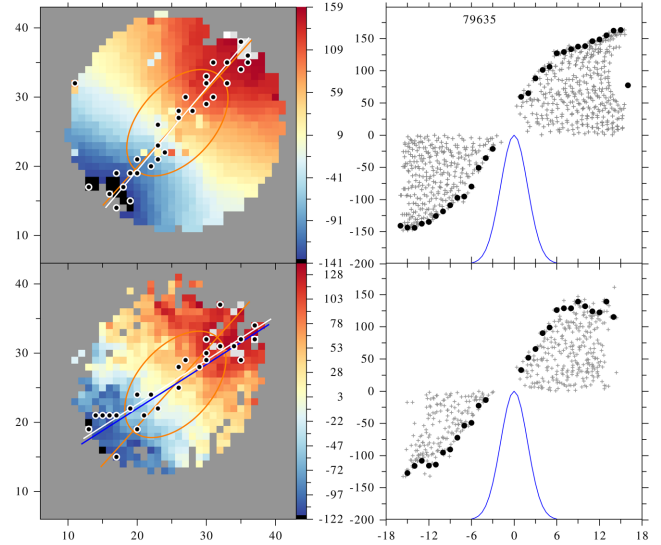
Figure 6. Example gaseous (top) versus stellar CSC from SAMI LZIFU fits. The pressure supported part of the stellar field is not shown. The kinematical LON is traced by the maximum LOS velocity within each elliptical annulus; all points in the cube are plotted at right within the envelope in bold. The major axis PSF is shown. Ellipse centres come from LZIFU fits to emission lines and from PPXF template fits to stellar absorption.
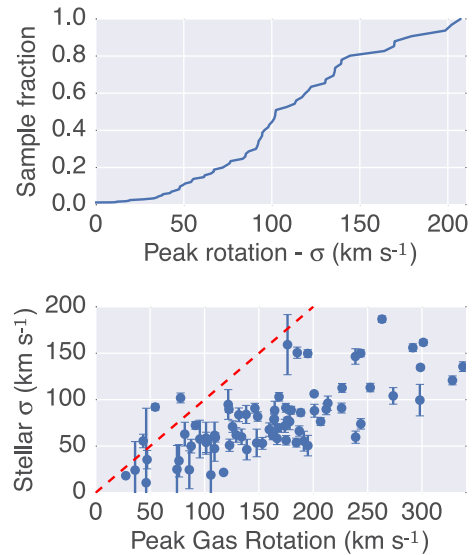
Figure 7. For some of our GAMA subsample averaged over the r_e ellipse, these plot the distribution in $\mathrm{km \, s^{-1}}$ of (top) gas peak CSC minus stellar σ, and (bottom) gas peak CSC derived by DISKFIT versus σ from PPXF fits to stellar absorption.

with mean 3.1 Gyr and dispersion 0.6 Gyr. For the GAMA subsample, Fig. 11(a) summarizes the distribution of median $\Upsilon_\times$ (2.6 median) and the product of this with the dereddened starlight extrapolated to $10 r_e$ to give the mass distributed like starlight while ignoring an IMF constraint. To recover some of the $\Upsilon_\star$ fits that failed (i.e. those with $b < 0$), we adjusted Υ to posit that unobserved baryons+DM distribute like starlight, namely as a very flattened mass homeoid. Indeed, this $\Upsilon_\times$ scheme fitted 37 of 42 failures of our CSCs (1/4), including three of our H I observed galaxies. Fig. 11(b) compares $\Upsilon_\times$ and $\Upsilon_\star$ from our fits in Fig. 9.
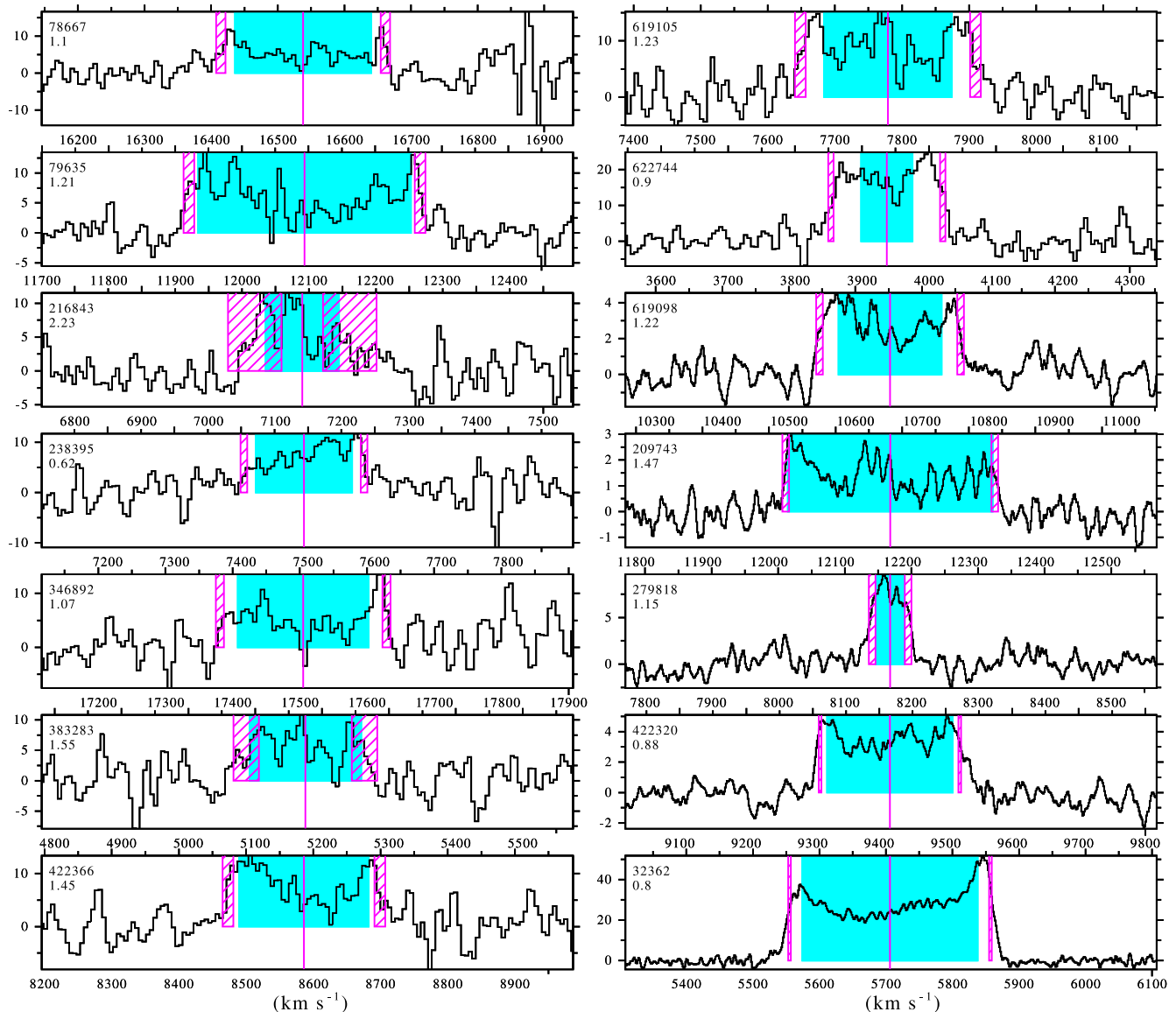
Figure 8. Representative ALFALFA survey H I profiles of SGS galaxies plus five longer Arecibo integrations at bottom right. Horizontal axis is heliocentric velocity (km s^{-1}), vertical axis is flux density (mJy) integrated over the 3.5 arcmin diameter beam. Cyan shades the velocity range of DISKFITS to flat discs of ionized gas. Magenta cross-hatches the W50 2σ extents of H I after correcting for 5 km s^{-1} FWHM spectral resolution. The number below the ID gives the asymmetry of flux integrated below/above systemic velocity.

Green in Fig. 9 shades the 5–95 per cent confidence interval of the $\Upsilon_\times$ fits. Most $\Upsilon_\times$ fits are good, but for the remaining ~10 per cent, our $\Upsilon_\star$ fit (using Salpeter IMF) exceeds $\Upsilon_\times$, an unphysical result, or the observed CSC deviated strongly at small and/or large radii from the scaled light CSC. Evidently in these, mass does not follow starlight.

3.4 Streaming

Even binned, many of our spectra could not map reliably h_3 and h_4 moments of the Gauss–Hermite parametrization of the stellar LOSVD, so we considered only gas streaming. Our ≳2 arcsec resolution prevented study of nuclear bars and rings, so we sought substantial non-axisymmetric features at least 3 arcsec long, ~5 kpc. The small areal coverage of SAMI compared to e.g. CALIFA pre-

vented determination of bar pattern-speed to locate resonances in the differentially rotating disc (Tremaine & Weinberg 1984). To maximize the number of points to compare the axisymmetric with non-axisymmetric fits, we considered the beam-smeared cubes, always allowing the bar major-axis PA to vary. Some photometric/kinematic fits co-aligned in PA, but χ^2 was often flat over 10 s of degrees in bar PA. That indeterminacy likely arose because some photometric asymmetries twisted in PA across the SAMI aperture, but tracking a twist was impractical with DISKFIT. For an acceptable non-axisymmetric fit, we required same-sign amplitudes for both the radial and tangential components of $m = 2$ streaming over >80 per cent of the fit uncertainty range.

Fig. 12 shows non-axisymmetric DISKFITS to 13 photometric asymmetries – bar candidates. Fig. 13 shows their angular modes and slightly non-circular streamlines. The Fourier modal analysis
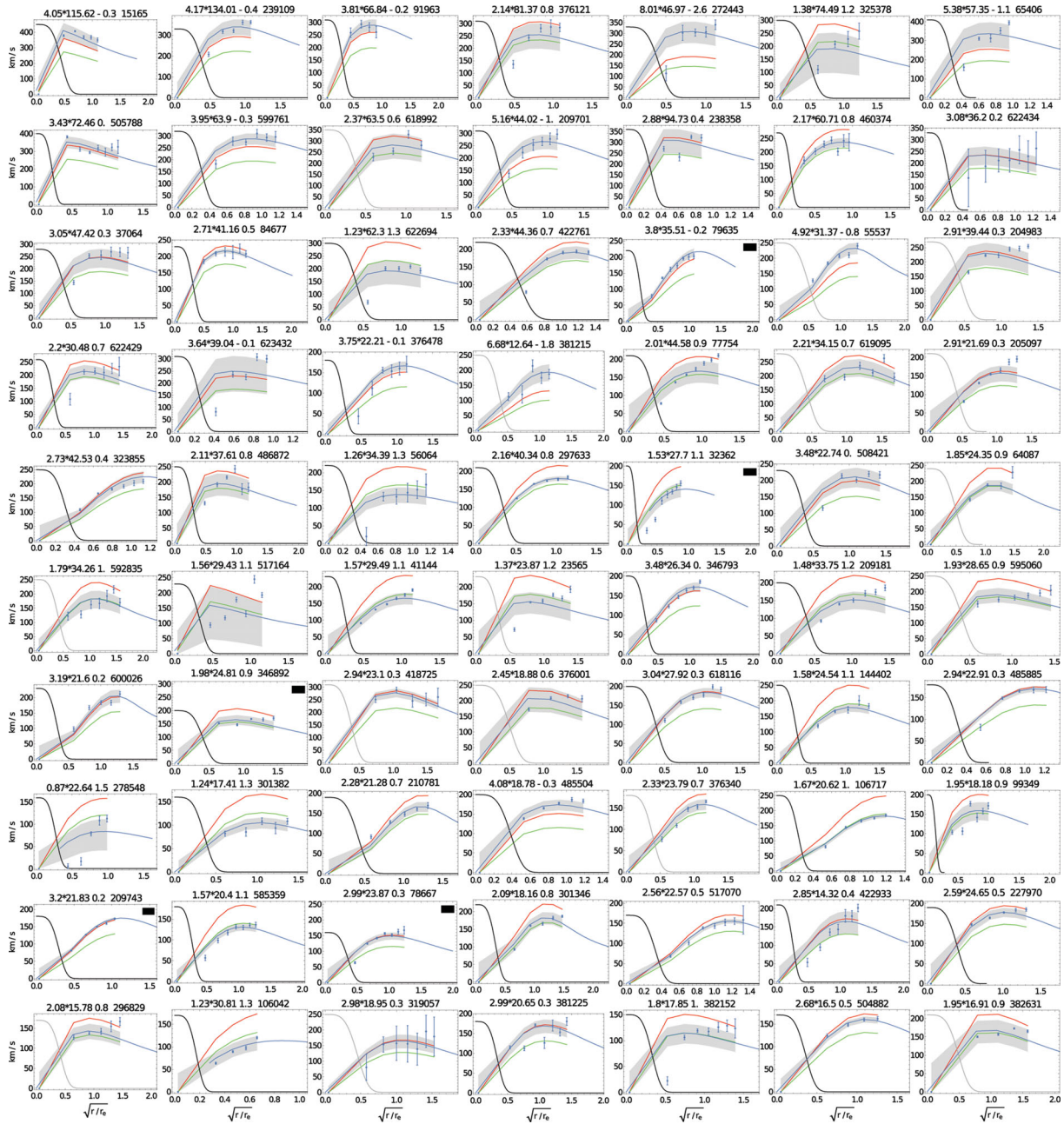
Figure 9. CSCs of our GAMA Survey subsample ordered by decreasing photometrically derived stellar mass; horizontal axis $\sqrt{r/r_e}$ emphasizes fits at small radii. The PSF is shown black for sharpest half and grey for the rest. Uncertainties at each radius span 5–95 per cent confidence. Green shades the confidence interval of the error-weighted linear fit to the CSC by the r-band single-Sérsic starlight profile of intrinsic flattening $q = 0.1$. The best-fitting blue line is extrapolated to the maximum radius of the successful Sérsic model to show the wedge that opens for DM+H I to flatten the CSC beyond. The black box on 14 CSCs spans vertically the uncertainty of the maximum rest-frame velocity of H I (Fig. 8). Atop each panel is listed the best-fit $\Upsilon_r \times$ dereddened stellar luminosity in units $10^9 M_\odot$ (Kennicutt, Tamblyn & Congdon 1994), historical star-formation parameter b for the best-fit Salpeter IMF, and the GAMA ID. $b > 1$ denotes an ongoing starburst, and $b < 0$ denotes a fit requiring DM. Red above green curves are the maximum amplitude CSCs generated by Salpeter and Kroupa IMFs for $b = 0$, respectively. When they lie below the shaded gray band, DM is required within the SAMI aperture.

detected such motions down to a few km s^{-1} in otherwise 'quiet' discs. Only 595060 and 376121 have in-plane streaming of >40 km s^{-1}, but still far below the shock velocities indicated by their emission line ratios (red overlays in Fig. 13). In several cases discussed in the appendix, streaming was more plausibly associated with strong spiral arms at larger radii than along a bar.

4 DISCUSSION

A flattened bulge may merge into the disc if it results from, or is substantially modified by, a bar where some stars and gas have non-circular orbits. $\Upsilon_\star$ may vary with radius. Gas turbulence can make a disc spatiokinematically 'lumpy'. We now assess these issues before considering DM.
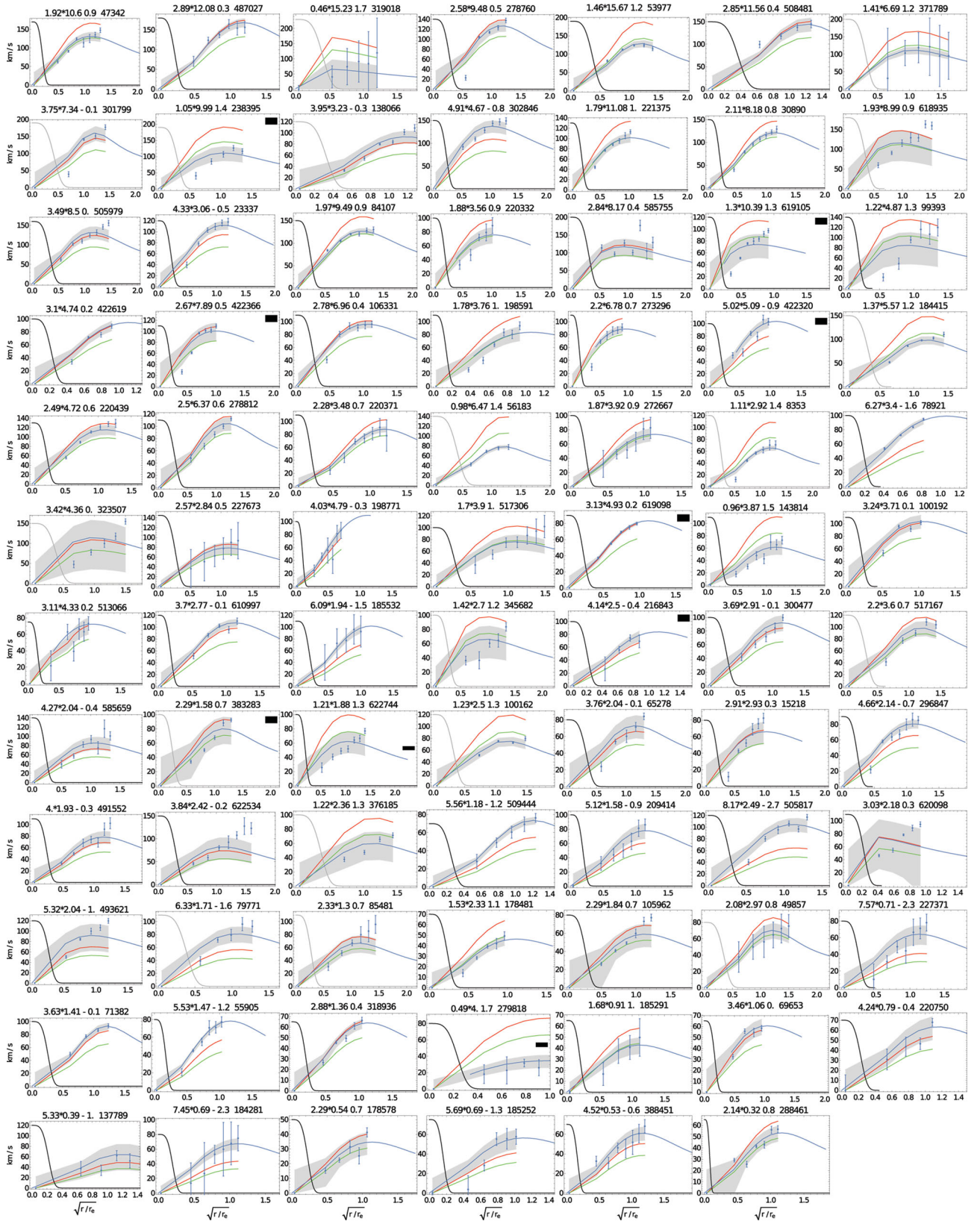
Figure 9 – *continued.*
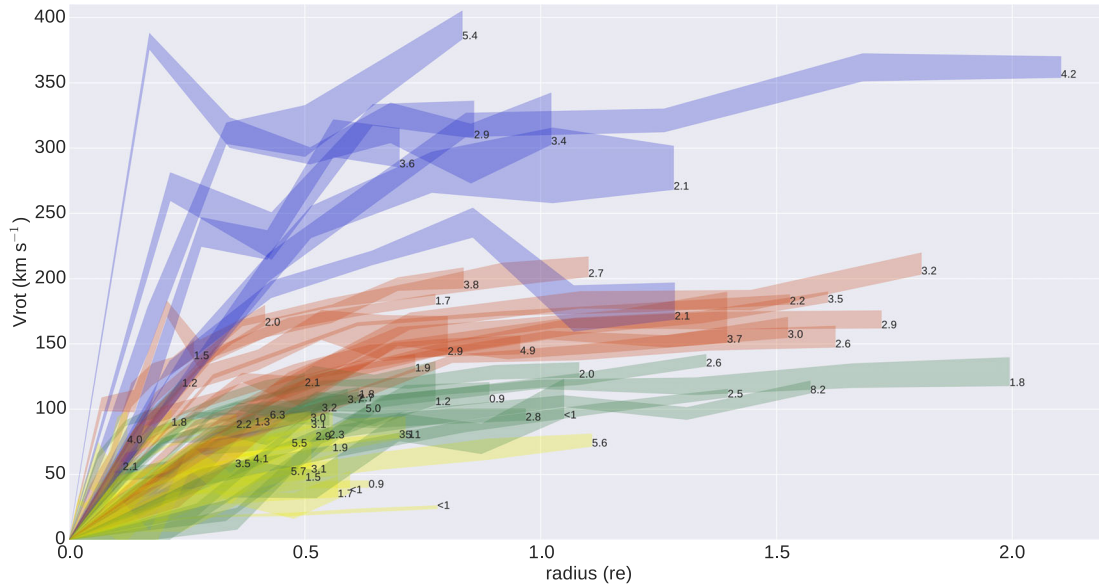
Figure 10. CSCs having median or smaller beam-smear; each is labelled by its median dynamical $\Upsilon_\times$ in solar units after dereddening and correcting for line emission within the r band. Horizontal axis is major-axis radius in Sérsic r_e scalelengths. CSC fit 9–95 per cent confidence bands are shown; colour shading merely attempts to reduce confusion.
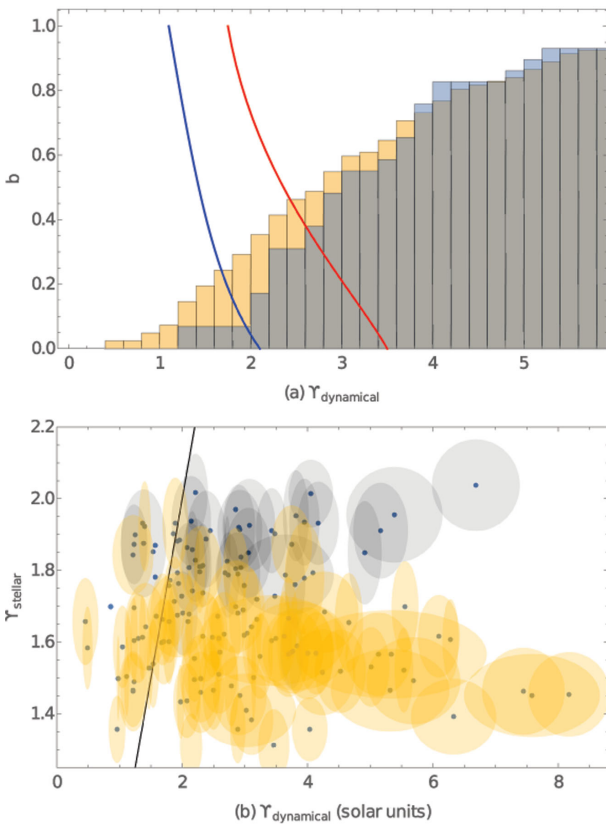
Figure 11. GAMA subsample (a) cumulative distribution of $\Upsilon_\times$. Grey shows systems of stellar mass $>10^{10.4}$ M$_\odot$, gold $<10^{10}$ M$_\odot$. Curves and vertical scale indicate the effect of Kennicutt et al. (1994) historical SFR parameter $b \equiv$ SFR$_{current}$/$\langle$SFR$\rangle_{past}$. CML model values to left of the red curve are valid for exponentially declining SFR with two IMFs from PST04 Fig. 4: red is Salpeter, blue is Kroupa. The 'diet Salpeter' IMF of Bell & de Jong (2001) falls between these. (b) IMF-unconstrained $\Upsilon_\times$ compared to Υ_P derived from stellar population fits across the brightest 40 per cent of a galaxy; uncertainty ellipses span 2σ. The two Υ measures are clearly uncorrelated.

4.1 Photometric versus gas/stellar kinematical PAs

Many galaxies show bars, especially in the near-infrared (at least 70 per cent; Eskridge et al. 2000). Sharper images reveal more nuclear bars, rings, and lenses with stars often forming in a central light cusp (e.g. Bureau & Freeman 1999). In 12 nearby discs, Seidel et al. (2015) find that strong bars do not alter global rotation, but the majority do have double peaks in stellar-rotational velocity along the kinematical major axis, and occasionally show central decreases in velocity dispersion probably from nuclear rings. Emsellem et al. (2007) probe velocity field irregularities and find a dip at ~1/4 bar length in the majority of their sample regardless of Hubble type and bar strength; this is the scale of the Inner Lindblad Resonance (Pfenniger & Norman 1990) that often coincides with a stellar ring or lens (e.g. Buta 2012, and references therein), but was often within the PSF of our bar candidates so could not be assessed.

Barrera-Ballesteros et al. (2014, BB14 hereafter) find $<14°$ differences between stellar and gaseous kinematical PAs for almost all of their barred sample from the CALIFA survey (Sánchez et al. 2012). Our Fig. 5 blue curve shows that 15 per cent of SGS GAMA subsample galaxies exceed that angle. The CALIFA PA fits span 24 ± 5 arcsec radii (Table 1 BB14), which is comparable to our fit extent because the SGS averages ~3 × the redshift of CALIFA (Fig. 2c).

BB14 find that 26/27 barred galaxies have kinematical versus photometric major axis PAs misaligned by $<20°$, like unbarred systems; the single large misalignment is attributed to external interaction. Our Fig. 5 red and green curves tested their conclusion. With more than triple their target number, we found that 5 per cent of our sample misaligned by $>30°$ yet show no evidence for a recent external influence.

Bar response of gas should exceed that of stars, e.g. strong bars in Seidel et al. (2015) have ~2.5 × the torque in gas than in stars. Epinat et al. (2008) found 15 per cent of spirals misaligned by $>15°$, our Fig. 5 confirms this fraction.

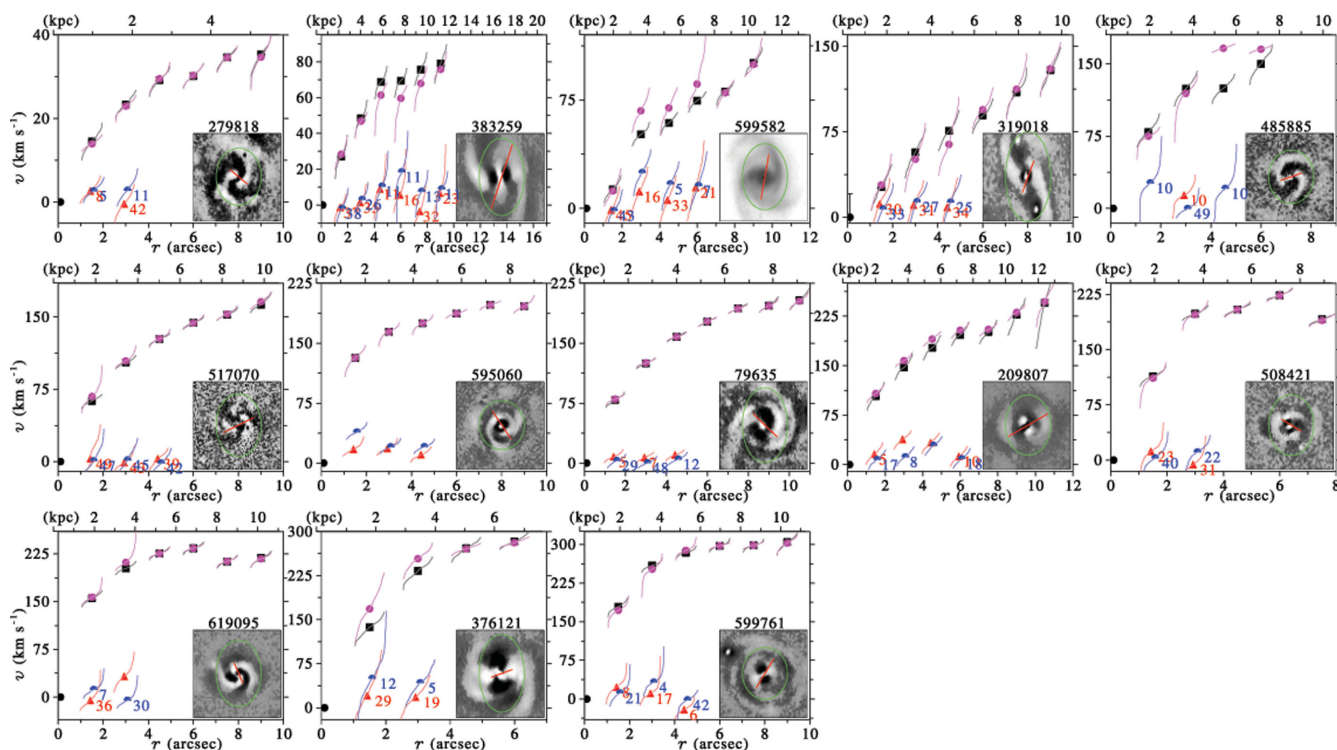In summary, deviated PAs are quite evident in the SGS, so we now consider how those flows influence the CSCs.

Figure 12. CSCs with (magenta) and without (black) streaming for systems with asymmetric VIKING Z-band residuals, ordered by increasing peak circular speed from top left to lower right. Inset figure has sqrt-scaled intensities after subtracting the best-fitting dual-Sérsic profile (see Fig. 13 for detail); 599582 as yet has no Sérsic Z-band fit so is shown unmodified. Images are oriented with kinematical major axis horizontal and are deprojected to face-on. SAMI spanned the green ellipse. The extent and orientation of the best-fitting kinematical distortion is shown by a red line. Each symbol is plotted at the median velocity of the cumulative uncertainty distribution at that radius, shown from 5 to 95 percentiles. Numbers on these distributions indicate the percentage below the $0\,\mathrm{km\,s^{-1}}$ (i.e. v_{sys}) line. Black squares plot the axisymmetric CSC, blue semi-circles plot radial streaming, red triangles plot tangential streaming, and magenta circles plot the barred $m = 0$ CSC; barred points are displaced slightly for clarity. Horizontal axis has arcsecond scale at bottom and kpc at top.

4.2 Weak influence on CSCs from common bars

Strong stellar bars can deviate gas by 30 to $>100\,\mathrm{km\,s^{-1}}$ from circular rotation along their leading edge (e.g. Sellwood & Zanmar-Sanchez 2010, using DISKFIT). Holmes et al. (2015) apply DISKFIT to the CALIFA galaxy survey DR1 (Sánchez et al. 2012), finding non-axisymmetric motions in 12/37 with 11/12 having bars. Yet, BB14 and Seidel et al. (2015) show that even stronger bars do not modify gas CSCs. An axisymmetric fit to a distorted velocity field will be biased low when the streaming distortion aligns near the disc major axis because gas there is at its orbit apogalacticon. Gas motions along our sightline increase when we view a bar end-on. It is therefore important to check with broad ranging samples that ionized gas moves in sufficiently circular orbits to trace mass density over the full ranges of galaxy environment and mass.

We found that the distortion of CSC by a bar was generally only 10–30 $\mathrm{km\,s^{-1}}$. The maximum amplitude may have shrunk because Figs 12 and 13 show that the photometric residuals twist in PA over the SAMI aperture, averaging extreme values over the fixed bar axis of our DISKFIT. Indeed, the presence of shock excited emission-lines in more than 2/3 of our galaxies with shock values up to several hundred $\mathrm{km\,s^{-1}}$ do imply that such motions are buried in our cubes.

In even our least smeared quartile, $m = 2$ distortions were compact, altering only two CSCs by >30 per cent amplitude at small radii as they built up (376121 and 209807).

Thus, asymmetries in the SGS did not undermine application of a CSC to mass studies, and support the assertion of e.g. Kormendy

(2012) that a locally increasing or flat CSC like all here inhibit secular disc evolution.

4.3 Mass decomposition

If nominal $\Upsilon_\star$ is increased ad hoc to avoid substantial DM (i.e. <25 per cent contribution to CSC) at radii up to peak velocity, i.e. our $\Upsilon_\times$ fits, even compact photometric features can have a kinematical counterpart (e.g. Corradi & Capaccioli 1990). Of course, a DM halo or MOND must still flatten the CSC in any outer H I disc beyond most starlight. In luminous SA galaxies, Noordermeer et al. (2007) find that the inner CSC shape correlates with the light distribution, so large bulges dominate dynamics. However, de Blok et al. (2008) find correlations even in Sb-c galaxies, likewise, Salucci, Yegorova & Drory (2008) obtain excellent starlight-only fits for 18 spirals within $3r_e$.

In contrast, such 'maximal discs' have been excluded in 30 nearly face-on galaxies by the DiskMass survey of vertical velocity dispersions (Martinsson et al. 2013). There, up to half of the disc mass may be DM. Likewise, the Milky Way Galaxy's CSC can be matched with 40 per cent DM within the inner 10 kpc (Portail et al. 2015).

Lacking H I maps to ~ 20 kpc (Sofue 2013), it was fruitless for us to specify a DM halo form for the 25 per cent that failed to fit with $\Upsilon_\star$, or the 10 per cent that $\Upsilon_\times$ failed to fit. Even with H I, one can play off luminous mass against a dark halo modified by uncertain compression (e.g. Dutton et al. 2005). For example, Noordermeer et al. (2007) isolate discs from large SA bulges to fit
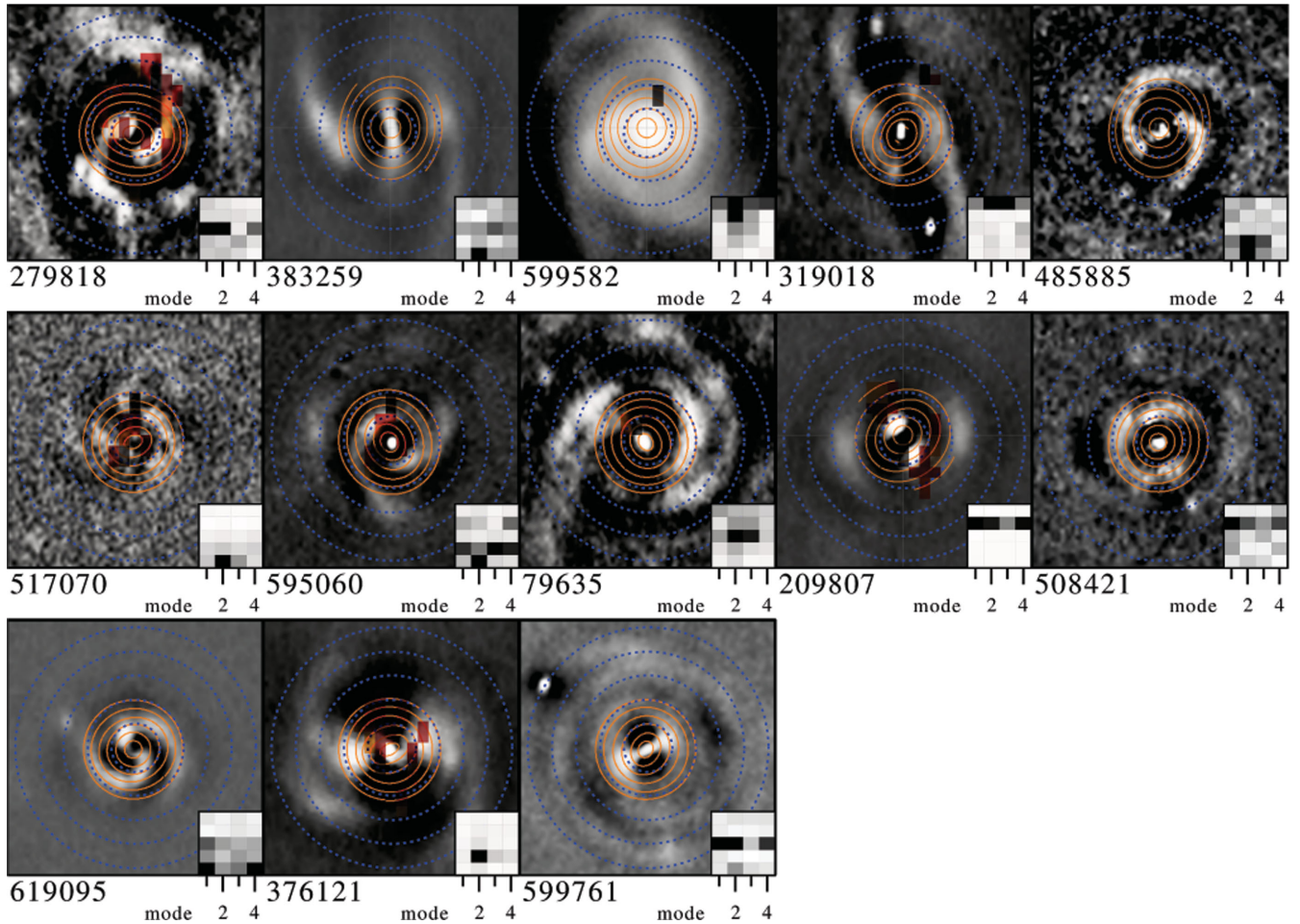
Figure 13. *Z*-band residuals after subtracting the best-fitting dual-Sérsic profile, deprojected to face-on using the inclination from the Sérsic single-profile fit, plotted with the kinematic major axis horizontal (37 arcsec extent), and showing in orange the streamlines of our best-fitting bar model gaseous velocity field over the SAMI extent left to right. 599582 as yet has no Sérsic *Z*-band fit so is shown unmodified. The inserts show modal content in each blue ring of 3.5 arcsec extent from centre at bottom; note sometimes strong $m = 2$ mode from bar (second radial bin) and arms (beyond). Coloured rectangles on several systems locate high-velocity (150 to 300 km s^{-1} from lighter to darker red) shocks as evidenced by diagnostic emission-line flux ratios.

CML $\Upsilon_R \sim 1$–10. Even with H I at larger radii, their fits are comparable using various DM distributions. They find that a spherical, isothermal halo generally fits better especially at >10 kpc, but they can fit a subset just by H I scaling. de Blok et al. (2008) are sensitive to DM halo details because their H I data are extensive. With this background, we now discuss our findings on $\Upsilon_\times$ then $\Upsilon_\star$.

4.3.1 Trends of dynamical and stellar M/L

As the distribution of luminous mass flattens, $V(r)$ increases while $\Upsilon V^2(r)$ remains constant, so Υ declines. As extremes, Takamiya & Sofue (2000) bound Υ_V by placing all mass in either a sphere or disc. They find that VML Υ_V on average at most doubles to ~10 solar from 2 kpc to our typical maximum extent of 10 kpc. This contradicts the chemophotometric models of PS10, whose disc VML $\Upsilon_\star(r)$ declines at larger radii and from smaller values $\lesssim 2.5$. Indeed, in all inside-out galaxy formation models, VML from stars declines with increasing radius from younger/less metallic stars there (e.g. Portinari & Salucci 2010, PS10 hereafter), but cannot generate the full amplitude of the CSC.

PS10 include a DM halo and fit Sb–Sc CSCs within $2R_{opt}$ equally well with either CML or VML, finding that a VML/CML

disc contributes less/more to the CSC hence mass and implies a larger/smaller DM core. More rapid mass build-up with radius draws the peak of the CSC inwards by ~25 per cent radius while boosting its amplitude ~10 per cent. The VML stellar mass profile is 20 per cent more centrally concentrated than the light.

With VML, PS10 predict an expanded region of 'inner baryon dominance' and suggest that it may also explain unusually strong radial colour gradients in some galaxies. They approximate the *I*-band stellar $\Upsilon_\star$ normalized at r_e by

$$\frac{\Upsilon_\star(r)}{\Upsilon_{\star,1}} = \exp\left\{ -\alpha(s)\left[\left(\frac{R}{h_I}\right)^s - 1\right]\right\} \tag{8}$$

with $\alpha(s) = 1.25(1.3 - s)^3 + 0.13$, and $s = 1 \pm 0.1$ for the 'shallow' form (essentially linear within $3r_e$) and 0.6 ± 0.1 for the 'concave' form ('cuspy' within $0.5r_e$). The bottom panel of PST04 Fig. 6 shows comparable spread between models in *R* band (almost our *r* band) but rising faster at small *b* than in *I* band.

Small r_es meant that we could not distinguish between these forms: uncertainty bands of our $\Upsilon_\times$ fits often spanned both. CML with either exponentially declining star formation rate (SFR) or Portinari, Sommer-Larsen & Tantalo (2004, hereafter PST04)

chemophotometric models both fitted our CSCs more often than did VML. Hence, we discuss only CML $\Upsilon_\times$ models, which merely up-scaled our Sérsic-fitted CSC.

4.3.2 Implications of our CML fits

Fig. 10 does not show a trend between the Υ and rotational peak velocity (mass) of the successful fits, e.g. lower mass systems do not have larger $\Upsilon_\star$.

Two-thirds of our $\Upsilon_\times$ distribution is consistent with CML for stars+remnants using various IMFs (example curves in Fig. 11a) in PST04 and exponentially declining SFR. For example, PST04 Fig. 5 attains $0.75 \lesssim \Upsilon_I \lesssim 3.4$ at solar or greater metallicity as Kennicutt et al. (1994) birthrate parameter b ranges from 1 to 0. Their table 7 shows $\Upsilon_I \sim 2.1 - 0.8$ for Sa-Sc discs, respectively. $\Upsilon_I < 0.75$ is for $b > 1$, i.e. star-bursting systems. Even the lower mass heavy Salpeter IMF cannot exceed $\Upsilon_r = 3.4$, so galaxies in the top 20 per cent of our distribution to right of the red curve require more than the stellar mass in unobserved baryons+DM close to $2r_e$. For the PST04 chemophotometric VML, all IMF curves shift leftwards, increasing needed matter within and somewhat beyond $\sim 2r_e$. $\Upsilon_\star$ from our stellar population fits unphysically exceeds the dynamically derived $\Upsilon_\times$ for only 10 per cent of our GAMA subsample. Excluding this group, the distribution agrees with the Salpeter IMF for all b in the PST04 models (red curve in Fig. 11a).

Kennicutt et al. (1994) find $b < 0.2$ for Sa-Sab discs, 0.3–0.4 for Sb, and 0.8–1 for Sbc-Sc. Therefore our two-thirds $\Upsilon_\times$ fit successes need few unobserved baryons and/or DM distributed similarly to starlight within 10 kpc radius. Our median $\Upsilon_\star$ implied 30–40 per cent of the starlight mass in H I, a global result weighted outside the SAMI aperture, which is consistent with most of the ALFALFA fluxes (Fig. 10). Fig. 11(a) shows that the few failures of $\Upsilon_\times$ in Fig. 9 imply different distributions of their mass and starlight.

5 CONCLUSIONS

We studied 178 galaxies in the SGS v0.9 release not close to edge- or face-on and lacking prominent r-band bars in SDSS images. We thus developed procedures to quantify CSCs and Υ_r for typical galaxies in the SGS having moderately distorted CSCs hence mostly circular orbits.

We used DISKFIT to map gas kinematics across the whole disc at once to highlight asymmetries and to trace the CSC. Fit uncertainties were estimated by boot-strapping over PA uncertainties always, sometimes light centre and, where appropriate, bar PA using GAMA Survey photometric priors; inclinations were always GAMA priors. We quantified $m = 2$ gas streaming along photometric asymmetries. We found statistically significant deviations of $< 40 \, \text{km s}^{-1}$ in 12 galaxies that however barely altered the CSC, and $80 \, \text{km s}^{-1}$ in one. In our sample, emission-line ratios often indicated shocks of several hundred km s^{-1}. The absence of velocity residuals of comparable amplitude was likely a result of compact shock fronts being blurred away by seeing. For the rest, adding $m = 1$ 'lop-sided' asymmetry did not improve fits. Many CSCs rose slowly through the SAMI aperture even after correcting for beam smearing within $0.5r_e$, to peak at 1–$2 \, r_e$ and 80–$300 \, \text{km s}^{-1}$. Amplitudes of 14 with representative H I velocity profiles almost always matched the peak of the SAMI CSC, so those CSCs do not rise beyond the SAMI aperture and are plausibly flat there.

We assumed that mass across the SAMI aperture was distributed in flattened, luminous nested homeoids, and quantified it dynami-

cally – modulo CML $\Upsilon_\times$ – from Sérsic profile fits to r-band SDSS photometry. After correcting luminosity down for line emission and up for average dust attenuation, two-thirds of the distribution of median $\Upsilon_\times$ (its median = 2.6) was compatible with plausible IMFs and Kennicutt et al. (1994) birthrate parameter b. We could fit the CSC of 37 more galaxies simply by up-scaling the starlight profile by a CML $\Upsilon_\times$. Thus, we inferred for those at most a comparable mass of unobserved baryons and/or DM distributed like starlight. For the remaining ~ 10 per cent, we needed mass distributed quite differently from starlight; more sophisticated population fits to SGS *spectra* using stellar VML may define the radial variations of this offset to isolate the DM. Our results demonstrate that the full SGS will be able to explore environmental effects on CSCs, Υ, and IMFs.

REFERENCES

Allen J. T. et al., 2015, MNRAS, 446, 1567

Amran P., Marcelin M., Balkowski C., Cayatte V., Sullivan W. T., III, Le Coarer E., 1994, A&A, 103, 5

Barrera-Ballesteros J. K. et al., 2014, A&A, 568, A70 (BB14)

Bell E., De Jong R. S., 2001, ApJ, 550, 212

Bertin E., 2013, Astrophysics Source Code Library, record ascl:1301.001

Bertin E., Arnouts S., 1995, A&A, 117, 393

Bland-Hawthorn J. et al., 2011, Optics Express, 19, 2649

Blanton M. R. et al., 2003, ApJ, 594, 186

Bryant J., Bland-Hawthorn J., Fogarty L. M. R., Lawrence J. S., Croom S. M., 2014, MNRAS, 438, 869

Bryant J. et al., 2015, MNRAS, 447, 2857

Bureau M., Freeman K. C., 1999, AJ, 118, 126

Buta R., 2012, in Falcón-Barroso J., Knapen J. H., eds, Chapter 2 in Secular Evolution of Galaxies. Cambridge Univ. Press, Cambridge

Buta R. J., Luarikainen E., Salo H., Block D. L., Knapen J. K., 2006, AJ, 132, 1859

Buta R. J., Corwin H. G., Odewahn S. C., 2007, The de Vaucouleurs Atlas of Galaxies. Cambridge Univ. Press, Cambridge

Calzetti D., 2001, PASP, 113, 1449

Cappellari M., Emsellem E., 2004, PASP, 116, 138

Catinella B., Giovanelli R., Haynes M. P., 2006, ApJ, 640, 751

Catinella B. et al., 2010, MNRAS, 403, 683

Catinella B. et al., 2013, MNRAS, 436, 34

Conroy C., 2013, ARA&A, 51, 393

Corradi R. L. M., Capaccioli M., 1990, A&A, 237, 36

Courteau S., 1997, AJ, 114, 6

Croom S. et al., 2012, MNRAS, 421, 872

de Blok W. J. G., Walter F., Brinks E., Trachternach C., Oh S.-H., Kennicutt R. C., Jr, 2008, AJ, 136, 2648

Driver S. et al., 2011, MNRAS, 413, 971

Dutton A. A., Courteau S., de Jong R., Carignan C., 2005, ApJ, 619, 218

Emsellem E. et al., 2007, MNRAS, 379, 401

Epinat B. et al., 2008, MNRAS, 388, 500

Eskridge P. B. et al., 2000, AJ, 119, 536

Fogarty L. M. R. et al., 2014, MNRAS, 443, 485

Gadotti D. A., de Souza R. E., 2005, ApJ, 629, 797

Giovanelli R. et al., 2005, AJ, 130, 2598

Haynes M. P. et al., 2011, AJ, 142, 170

Hoekstra H., van Albada T. S., Sancisi R., 2001, MNRAS, 323, 453

Ho I.-T. et al., 2014, MNRAS, 444, 3894

Holmes L. et al., 2015, MNRAS, 451, 4397

Kelvin L., 2013, PhD thesis, Univ. St. Andrews

Kelvin L. et al., 2012, MNRAS, 421, 1007

Kennicutt R. C., Tamblyn P., Congdon C. W., 1994, ApJ, 435, 22

Kormendy J., 2012, in Falcón-Barroso J., Knapen J. H., eds, Chapter 1 in Secular Evolution of Galaxies. Cambridge University Press, Cambridge

Kormendy J., Kennicutt R. C., 2004, ARA&A, 42, 603

Kroupa P., 2002, Science, 295, 82

Lange R. et al., 2015, MNRAS, 447, 2603

Lawrence A. et al., 2007, MNRAS, 379, 1599L

McGaugh S. S., Schombert J. M., Bothun G. D., de Blok W. j. G., 2000, ApJ, 533, L99

McGaugh S. S., Schombert J. M., de blok W. J. G., and Zagursky M. J., 2010, ApJ, 708, L14

Martinsson T. P. K., Verheijen M. A. W., Westfall K. B., Bershady M. A., Andersen D. R., Swaters R. A., 2013, A&A, 557, 131

Milgrom M., 1983, ApJ, 270, 365

Noordermeer E., 2008, MNRAS, 385, 1359

Noordermeer E., van der Hulst J. M., Sancisi R., Swaters R. S., van Albada T. S., 2007, MNRAS, 376, 1513

Peng C. Y., Ho L. C., Impey C. D., Rix H.-W., 2010, AJ, 139, 2097

Pfenniger D., Norman C., 1990, ApJ, 363, 391

Pfenniger D., Revaz Y., 2005, A&A, 431, 511

Portail M., Wegg C., Gerhard O., Martinez-Valpuesta I., 2015, MNRAS, 448, 713

Portinari L., Salucci P., 2010, A&A, 521, A82 (PS10)

Portinari L., Sommer-Larsen J., Tantalo R., 2004, MNRAS, 347, 691 (PST04)

Rubin V. C., Burstein D., Ford W. K., Jr, Thonnard N., 1985, ApJ, 289, 81

Salucci P., Yegorova I. A., Drory N., 2008, MNRAS, 388, 159

Sánchez, S. F. et al., 2012, A&A, 538, A8

Sánchez-Blázquez P., Peletier R. F., Jimnez-Vicente J., Cardiel N., Cenarro A. J., Falcn-Barroso J., Gorgas J., Selam S., Vazdekis A., 2006, MNRAS, 371, 703

Sancisi R., 1976, A&A, 53, 159

Sanders R. H., 1996, ApJ, 473, 117

Schaefer A. et al., 2015, MNRAS, submitted

Schlafly E. F., Finkbeiner D. P., 2011, ApJ, 737, 103

Seidel M. K. et al., MNRAS, in press

Sellwood J., Spekkens C., 2007, ApJ, 664, 204

Sellwood J. A., Zanmar-Sanchez R., 2010, MNRAS, 494, 1735

Sharp R. et al., 2014, MNRAS, 446, 1551

Sofue Y., 2013, Planets, Stars and Stellar Systems Vol. 5. Springer Science+Business Media, Dordrecht

Sofue Y., Rubin V., 2001, ARA&A, 38, 137

Sofue Y., Tutui Y., Honma M., Tomita A., Takamiya T., Koda J., Takeda Y., 1999, ApJ, 523, 136

Staveley-Smith L., Bland J., Axon D. J., Davies R. D., Sharples R. M., 1990, ApJ, 364, 23

Sutherland R. S., Dopita M. A. D., 2003, ApJS, 8, 253

Takamiya T., Sofue Y., 2000, ApJ, 534, 670

Taylor E. N. et al., 2011, MNRAS, 418, 158

Tremaine S., Weinberg M., 1984, ApJ, 282, L5

Verheijen M. A. W., Sancisi R., 2001, A&A, 370, 765

APPENDIX

Here, we summarize properties of some GAMA subsample galaxies showing significant *r*-band photometric asymmetries after subtracting a single-Sérsic profile. We distinguish between those with and without streaming by bars or spiral arms, ordered as in Figs 12 and 13 from smallest to largest peak CSC velocity. As noted below, DISKFIT sometimes found no kinematical distortions as evidenced by opposite signs for $V_{2,r}$ and $V_{2,t}$ regardless of prior bar PA and extent chosen. For those, Fig. 12 shows the result aligned with the photometric feature to gauge uncertainties. Where feasible, we classified morphology (Buta et al. 2007; Kormendy 2012), with the caveat that SDSS and VIKING images are too shallow to see outer rings that would anyway be outside the SAMI aperture. Fig. 13 shows the deprojected, face-on, square-root intensity scaled, non-axisymmetric residuals after subtracting the dual-Sérsic fitted profile. We also show the best-fitting elliptical streamlines and modal content. In general, the CSC is rarely modified at even the bar radii.

Unless noted, emission-line flux ratios (generally [S II]/Hα versus [O III]/Hβ) indicate insignificant gaseous excitation by shocks, unsurprising given the generally low $m = 2$ in-plane velocities from our fits (with uncertainties from spatial averaging over kinematical twists). Deviant velocities mentioned have been projected into the disc plane. Shocks noted have emission line ratios consistent with shock velocities of 150–300 km s^{-1} and are deprojected as red tint rectangles in Fig. 13. Radial extents on sky are reported. A large span in $m = 2$ uncertainties in Fig. 12 generally arose when the kinematic centre and/or bar PA were unconstrained in our fit. The latter could occur when our fits were averaged by being constrained inappropriately to follow a fixed kinematical PA.

279818 – a 'flocculent' Sc with $\log_{10}(M_{\rm H I}/M_{\odot}) = 9.35$; only 10 per cent H I profile flux asymmetry. $m = 2$ reached only ~5 km s^{-1} at 3 arcsec along PA 3°, so was consistent with spiral-arm streaming. Stubby arms spiral from the bar tips, where emission-line flux ratios indicate shock excitation that is inconsistent with the tiny streaming.

383259 – SB(s) with perpendicular bar-within-bar, a good candidate to study at higher spatial resolution. For Fig. 12, we fixed the bar PA at the 6 arcsec scale along PA 135°. Despite the

photometrically strong bars, streaming amplitudes are $<20\,\mathrm{km\,s^{-1}}$. $\log_{10}(M_{\mathrm{H_I}}/\mathrm{M_\odot}) = 10.18$.

599582 – single-Sérsic fit only, because the bar along PA 165° is embedded in a strong lens and transects a ring, classic SB(r). A few spaxels show shock excitation.

319018 – a compact bulge SB(s) has knots aligned along PA 150° after the second Sérsic is subtracted, as frequently seen at bar *ansae* (e.g. Kormendy 2012).

485885 – non-axisymmetric motions at 2–3 arcsec along PA 15° reached 30 km s^{-1}, but were perpendicular to the photometric bar, we detected streaming by the strong bisymmetric spiral arms in this SB(s).

595060 – SB(rs) with weak bar out to 3 arcsec along PA 45°. $m = 2$ declines from 35 km s^{-1} as radius increases. Shock emission is evident on this scale. Beyond the bar there are residuals of $\sim$8 km s^{-1} along the spiral arms.

209807 – if the $m = 2$ distortion PA is allowed to vary, the fit PA is indeterminate over 58±21° hence produces uncertain velocities with medians that reach 30 km s^{-1}. This perhaps SB(rs) shows shock excitation at the ends of the bar.

619095 – prominent bar in this SB(s) along PA 110° with weak bar motions out to 3 arcsec. Residuals of $\sim$18 km s^{-1} are found along the spiral arms.

376121 – in this SAB(s), the bar emerges from a compact bulge along PA −5°. $m = 2$ deviations are $\sim$80 km s^{-1} at the edge of the SAMI PSF then drop abruptly to remain $<$30 km s^{-1} out to 5 arcsec. Significant shock excitation is evident out to 5 arcsec.

599761 – bar along PA 30° out to 3 arcsec in this SB(s), maximum deviation 20 km s^{-1}.

Galaxies with photometric asymmetries but no bar streaming detected:

517070 – compact bulge with bar along PA 115° that crosses a ring, SB(rs). Shock excitation along one spiral arm but not near the bar.

79635 – SAB(r) with weak bar out to 4 arcsec along PA 90° but $m = 2$ motions are in the noise. There are residuals of $\sim$10 km s^{-1} along the spiral arms. $\log_{10}(M_{\mathrm{H_I}}/\mathrm{M_\odot}) = 10.21$, 20 per cent profile flux asymmetry.

508421 – prominent bar out to 3 arcsec along PA 55°, surrounded by broken ring, SB(r).

227572 – SB(s). Dual-Sérsic fit indicates a bar along PA 170°.

209181 – weak bar.

209701 – prominent bar residual in this SB(r) along PA 20°, out to 3 arcsec photometrically but $<$10 km s^{-1} residuals.

This paper has been typeset from a TEX/LATEX file prepared by the author.